

Computational Analysis of Interfacial Dynamics in Angled Hele-Shaw Cells: Instability Regimes

Daihui Lu, Federico Municchi* and Ivan C. Christov[†]

*School of Mechanical Engineering, Purdue University,
West Lafayette, Indiana 47907, USA*

March 10, 2024

Abstract

We present a theoretical and numerical study on the (in)stability of the interface between two immiscible liquids, i.e., viscous fingering, in angled Hele-Shaw cells across a range of capillary numbers (Ca). We consider two types of angled Hele-Shaw cells: diverging cells with a positive depth gradient and converging cells with a negative depth gradient, and compare those against parallel cells without a depth gradient. A modified linear stability analysis is employed to derive an expression for the growth rate of perturbations on the interface and for the critical capillary number (Ca_c) for such tapered Hele-Shaw cells with small gap gradients. Based on this new expression for Ca_c , a three-regime theory is formulated to describe the interface (in)stability: (i) in Regime I, the growth rate is always negative, thus the interface is stable; (ii) in Regime II, the growth rate remains zero (parallel cells), changes from negative to positive (converging cells), or from positive to negative (diverging cells), thus the interface (in)stability possibly changes type at some location in the cell; (iii) in Regime III, the growth rate is always positive, thus the interface is unstable. We conduct three-dimensional direct numerical simulations of the full Navier–Stokes equations, using a phase field method to enforce surface tension at the interface, to verify the theory and explore the effect of depth gradient on the interface (in)stability. We demonstrate that the depth gradient has only a slight influence in Regime I, and its effect is most pronounced in Regime III. Finally, we provide a critical discussion of the stability diagram derived from theoretical considerations versus the one obtained from direct numerical simulations.

Keywords: Saffman–Taylor instability; variable-depth fracture; linear stability analysis; interFoam simulation

1 Introduction

Secondary and enhanced oil recovery (EOR) require the stable displacement of flowing subsurface hydrocarbons by an injected fluid (Lake, 1989). Water, being abundant, is a typical choice of displacing fluid. However, it is well known that this displacement process is unstable due to the lower viscosity of water (even with various surfactants and additives mixed into it) compared to immiscible subsurface hydrocarbons (e.g., crude oil) (Hill, 1952, Saffman and Taylor, 1958, Chuoke et al., 1959). Consequently, “the average oil recovery factor worldwide is only between 20% and 40%” even accounting for modern EOR techniques (Muggeridge et al., 2014). Therefore, there is an ongoing need to better understand fluid–fluid interface instabilities in the presence of a viscosity contrast and surface tension. An additional complication, beyond the physicochemical properties of the fluids used in EOR, is that subsurface formations, from which hydrocarbons are to be extracted, are naturally heterogeneous with geometric variations in the flow passages (Jackson et al., 2003). In this regard, recent experiments (Al-Housseiny et al., 2012), which employed the Hele-Shaw analogy for modeling the conductivity of shaped fractures (Zimmerman and Bodvarsson, 1996), have re-emphasized the importance of understanding the effect of geometric on the stability of fluid–fluid interfaces in the subsurface.

*Present address: School of Mathematical Sciences, The University of Nottingham, University Park, Nottingham, NG7 2RD, UK.

[†]To whom the correspondence should be addressed. christov@purdue.edu; <http://tmnt-lab.org>

A similar problem arises during modern hydraulic fracturing (“fracking”) processes as well. Although the effectiveness of fracking was demonstrated in 1947 (Economides and Nolte, 2000), it remains a challenging approach to energy production, in particular, due to the complex thermo-hydro-mechanical-chemical coupled processes involved across multiple space and time scales (Hyman *et al.*, 2016). In this case, the displacing fluid, primarily water with proppants (Yew and Weng, 2014, Osipstov, 2017), is injected into a wellbore at high pressure to create cracks in the subsurface rock formation. The natural heterogeneity and geometric variations of flow passages in these formations thus become even more pronounced during fracking. Once again, the instability of the interface between the fracking (displacing) fluid and the hydrocarbons (defending, or displaced, fluid) must be managed to ensure a high oil recovery rate, especially during overflushing (Osipstov *et al.*, 2018). As with EOR, it is desirable to displace a stable interface through the fractured rock so as to produce a “clean” sweep of the fracture, minimizing the oil or gas film layers left behind. Thus, there is an impetus to study fluid–fluid interface instabilities in complex/variable geometries, which is subject of the present work.

1.1 Context for studying interfacial instabilities

Interfacial instabilities characterized by the competition of surface tension and flow are quite common in nature and industry: the formation of snow flakes during solidification of a liquid (Langer, 1980), “ribbing” in coating flows due to the variable gap between two rollers (Weinstein and Ruschak, 2004), breakup of liquid threads confined in microfluidic devices for the generation of emulsions (Anna, 2016) or for inkjet printing (Basaran *et al.*, 2013), and even in electromechanical systems such as flow batteries (Chen *et al.*, 2016), to list a few. In most (but not) all of these examples, the instabilities are caused by a viscosity contrast at the fluid–fluid interface (Homsy, 1987). Finger-like patterns form as the unstable interface grows, which has led to this phenomenon being termed *viscous fingering* (Saffman, 1986).

In the 1950s, Hill (1952), Saffman and Taylor (1958), and Chuoke *et al.* (1959) laid the foundations for the study of viscous fingering through both theoretical analysis and experiments. Specifically, Hill (1952) performed a one-dimensional (1D) stability analysis and conducted quantitative experiments for both stable and unstable interfaces between sugar liquors and water. Saffman and Taylor (1958) considered a less viscous fluid (air) displacing a more viscous one (glycerine) in a Hele-Shaw cell, i.e., a thin gap between two closely spaced flat plates, and predicted the finger’s growth rate via *linear stability analysis*. Saffman and Taylor (1958) additionally predicted and verified that when a single finger forms in a Hele-Shaw cell, it occupies almost exactly half the width of the cell, for most experiments, which was later supported by the theory of Pitts (1980). Since then, Saffman and Taylor’s approach has enabled a significant amount of theoretical and experimental research on interfacial instabilities.

1.2 Control of interfacial instabilities

Pearson (1960) (as well as a parallel work by Pitts and Greiller (1961)) analyzed the effect of a gap gradient on the Saffman–Taylor problem (Saffman and Taylor, 1958), in the context of thin films between rollers and spreaders. More recently, however, this problem has received renewed attention (Al-Housseiny *et al.*, 2012) due to the analogy between flow in a Hele-Shaw cell and flow through shaped subsurface fractures (Zimmerman and Bodvarsson, 1996) as well as flows in certain porous media (Bear, 1972, Homsy, 1987).

Specifically, due to the importance of interfacial instabilities (such as viscous fingering) in confined geometries across many applications, attempts to control them via stabilizing gradients have been made (Maxworthy, 2002). To this end, the linear stability analysis in the presence of a gap gradient (i.e., in an angle Hele-Shaw cell) was re-interpreted as a possible stabilization (control) mechanism (Al-Housseiny *et al.*, 2012). Zhao *et al.* (1992) previously revisited Pearson’s problem experimentally and Dias and Miranda (2010b) had updated the linear stability analysis to predict tip-splitting in the presence of variations of the flow passage.

Since then, an explosion of works has analyzed a variety of related interfacial instability problems in “non-standard” Hele-Shaw configurations (Morrow *et al.*, 2019), both fixed geometries (Dias and Miranda, 2013, Al-Housseiny *et al.*, 2012, Al-Housseiny and Stone, 2013, Hu *et al.*, 2016, Jackson *et al.*, 2017, Grenfell-Shaw and Woods, 2017, Bongrand and Tsai, 2018) and those with flow-driven geometric changes (Pihler-Puzović *et al.*, 2012, Al-Housseiny *et al.*, 2013, Pihler-Puzović *et al.*, 2013). Further variants on the same problem also include controlling the injection flow rate (Dias and Miranda, 2010a, Dias *et al.*, 2010, 2012), changing

the permeability by adjusting the structure of the porous medium (Jackson *et al.*, 2017, Rabbani *et al.*, 2018, Brandão *et al.*, 2018), applying an external force via rotation of the geometry or through a magnetic field (Carrillo *et al.*, 1996, Alvarez-Lacalle *et al.*, 2003, Miranda and Alvarez-Lacalle, 2005, Anjos *et al.*, 2018b), changing the fluid properties through the viscosity ratio (Anjos *et al.*, 2017), using non-Newtonian fluids (Vlad and Maher, 2000, Lindner *et al.*, 2002, Tordjeman, 2007, Boronin *et al.*, 2015) or even adding a suspended particulate phase (Xu *et al.*, 2016, Kim *et al.*, 2017).

We are interested in geometric controls. To this end, there are three primary ways to alter the physical geometry of an experimental Hele-Shaw apparatus: (i) creating a gradient along the flow direction by relaxing the requirement that the plates be parallel (Zhao *et al.*, 1992, Dias and Miranda, 2010b, Al-Housseiny *et al.*, 2012, Al-Housseiny and Stone, 2013, Bongrand and Tsai, 2018, Anjos *et al.*, 2018a, Morrow *et al.*, 2019); (ii) using an elastic membrane (that deforms due to flow underneath it) instead of a solid top plate (Pihler-Puzović *et al.*, 2012, Al-Housseiny *et al.*, 2013, Pihler-Puzović *et al.*, 2013); and (iii) lifting one of the plates in a time dependent manner (Dias and Miranda, 2010a, Zheng *et al.*, 2015, Díaz-Piola *et al.*, 2017). Among these possibilities, the case of a geometric gradient in the flow direction has attracted special attention because it naturally imitates the non-uniform, fractured subsurface flow passages (Muggeridge *et al.*, 2014, Osipov, 2017). The gradient could be (a) positive for an increasing gap depth in the flow direction (termed a *diverging* Hele-Shaw cell), or (b) negative for a decreasing gap depth (termed a *converging* cell).

1.3 Goals and outline of this work

Currently, despite extensive research on the topic, the predictions of mathematical analysis of the interfacial stability in tapered geometries (or attendant 2D numerical simulations) have not been verified through three-dimensional (3D) direct numerical simulation (DNS) of flow and interfacial instability. In fact, a study by Dong *et al.* (2011) concluded that a “3D [numerical] model is preferred to obtain a better comparison with experimental results.” Indeed, in 3D DNS, unlike physical experiments or the numerous previous simulations of the depth-averaged Hele-Shaw equations, we have control over the entire problem setup, which allows us to capture the full physics of the problem. The goal of this paper is to fill this knowledge gap for rectangular Hele-Shaw cells with nonuniform gap thickness by: (i) extending the linear stability theory of interfacial instability in Hele-Shaw cell with clear fluids by taking into account the local streamwise variation of parameters (e.g., capillary number, depth of the cell, and so on); (ii) supplementing and verifying the theoretical analysis with “full” 3D DNS.

To this end, this paper is organized as follows. In Sec. 2, we derive the (growth) decay rate of a (un)stable fluid–fluid interface between two immiscible phases in a Hele-Shaw with variable gap thickness (but constant gap gradient) via linear stability theory. Specifically, starting with Darcy’s equation (i.e., the depth-averaged momentum equation) and the continuity equation, we obtain a Laplace equation for pressure. By solving the latter, we find the pressure jump at the fluid–fluid interface, and we match this pressure jump to the one found from the Young–Laplace equation. Thus, we arrive at the growth rate of the interface. On the basis of this mathematical result, we then classify the interface stability into three flow regimes depending on the difference between a critical capillary number and inlet or outlet capillary numbers, generalizing previous work on this problem by Al-Housseiny *et al.* (2012). Next, in Sec. 4.1, we perform a series of DNSs (the methodology for which is described in Sec. 3) in a specific set of Hele-Shaw geometries. We use the simulations to verify our mathematical model (i.e., the theory developed in Sec. 2) for the growth rate of the interface. Then, in Sec. 4.2, we discuss the effect of the gap gradient on the stability based on the theoretical solution and further numerical experiments. In Sec. 4.3, we compare and discuss the flow regimes maps (in the 2D parameter space defined by the capillary number and the gap gradient) determined by theoretical and numerical analyses. Finally, conclusions stated and avenues for future work are discussed in Sec. 5.

2 Linear stability analysis

Consider two immiscible and incompressible viscous fluids flowing in a narrow gap between two rigid plates (see Fig. 1) with a constant depth gradient α . The depth of the cell $h(x) = h_{in} + \alpha x$ satisfies $\max_x h(x) \ll W$ and $\max_x h(x) \ll L$. Although we neglect gravity, in Fig. 1 it would act in the negative z -direction. The flow is in the x -direction, and the Hele-Shaw cell’s gap thickness, $h(x)$, only varies in this direction. The densities and viscosities of the displacing and defending fluids are denoted respectively as ρ_1, μ_1 and ρ_2, μ_2 . A fully

developed flow of fluid 1 (the displacing fluid), with an average (in the y - z cross-section) velocity U_{in} , pushes into a quiescent fluid 2 (the defending fluid). Between the two fluids there exists an interface that, due to immiscibility, is endowed with surface tension γ . The interface is not necessarily flat, and its shape is given by $x = \zeta(y, t)$. The horizontal direction perpendicular to the flow, i.e., the y -direction in Fig. 1, is assumed to be large compared to the typical gap size. Therefore, consistent with the linear stability analysis to be carried out below (and also previous work of [Al-Housseiny et al. \(2012\)](#), [Miranda and Widom \(1998\)](#)), we consider the interface to be periodic in y . Specifically, we shall apply a full-period initial perturbation to an initially flat interface to respect the periodic boundary conditions (PBCs) at $y = 0$ and $y = W$. Experiments have shown that PBCs have a similar effect to physical sidewalls in a cylindrical Hele-Shaw cell ([Zhao and Maher, 1990](#)), i.e., two coaxial cylinders separated by a small gap.

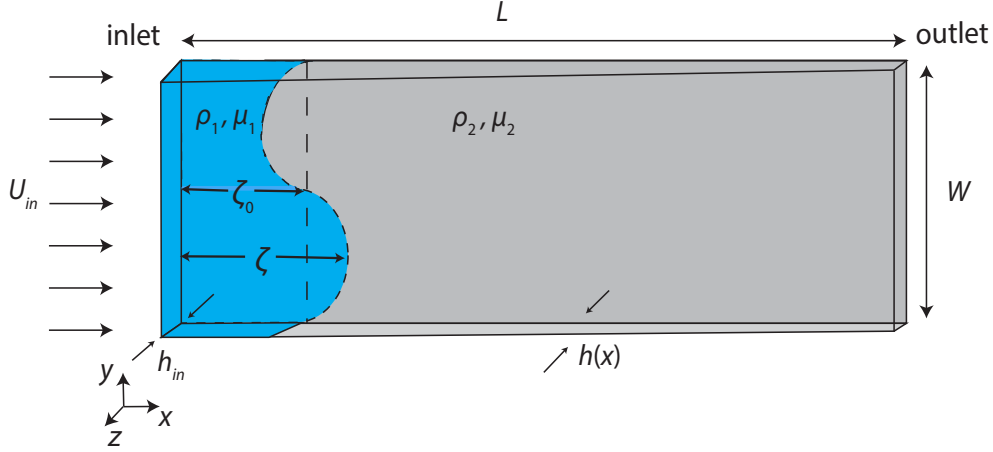


Figure 1: Top view schematic configuration of the flow in a rectilinear Hele-Shaw cell with a constant depth gradient α . The depth of the cell, $h(x) = h_{in} + \alpha x$, satisfies $\max_x h(x) \ll W$ and $\max_x h(x) \ll L$ and h_{in} is the depth at the inlet. Although we neglect gravity, in this view it would act in the negative z -direction. The flow is in the x -direction, and the Hele-Shaw cell's gap thickness, $h(x)$, only varies in this direction.

2.1 Linear growth rate

Following [Al-Housseiny and Stone \(2013\)](#), we start our linear stability analysis with the 2D (i.e., depth- or z -averaged) governing equations for the viscous fluid flow in the thin gap between two closely spaced plates ([Panton, 2013](#)):

$$\mathbf{u}_j = -\frac{h^2}{12\mu_j} \nabla p_j, \quad (1)$$

where the subscript $j = 1, 2$ represents the displacing and defending fluid, respectively; \mathbf{u}_j is the depth-averaged velocity field of fluid j in the (x, y) plane, p_j is the pressure field of fluid j , while h and μ_j were defined above (see also Fig. 1). Equation (1) is supplemented by the continuity (conservation of mass) equation for each incompressible fluid phase:

$$\nabla \cdot (h\mathbf{u}_j) = 0. \quad (2)$$

The flow has been assumed to be fully developed and steady.

Substituting Eq. (1) into Eq. (2), we obtain the governing equation for the pressure in each fluid

$$\nabla^2 p_j + \frac{3\alpha}{h(x)} \frac{\partial p_j}{\partial x} = 0. \quad (3)$$

In an angled Hele-Shaw cell, the depth is $h(x) = h_{in} + \alpha x$, so

$$\frac{1}{h(x)} = \frac{1}{h_{in} + \alpha x} = \frac{1}{h_{in}} - \frac{\alpha x}{h_{in}^2} + \mathcal{O}(\alpha^2). \quad (4)$$

Substituting Eq. (4) back into Eq. (3), and neglecting the $\mathcal{O}(\alpha^2)$ terms (consistent with the lubrication approximation under which Eq. (1) is derived (see, e.g., [Panton, 2013](#))), the pressure equation now has constant coefficients:

$$\frac{\partial^2 p_j}{\partial x^2} + \frac{\partial^2 p_j}{\partial y^2} + \frac{3\alpha}{h_{in}} \frac{\partial p_j}{\partial x} = 0 \quad (\alpha \ll 1). \quad (5)$$

Next, assume a flat base state for the (unperturbed) interface shape, denoted $\zeta(y, t) = \zeta_0(t)$. Then, we express the perturbed interface as a Fourier series:

$$\zeta(y, t) = \zeta_0(t) + \sum_{n \neq 0} \epsilon_n a_n e^{ik_n y + \lambda_n(t)}, \quad (6)$$

which satisfies the condition of periodic boundary conditions (PBCs) in y . In Eq. (6), the time derivative of $\lambda_n(t)$, denoted henceforth as λ_n and not necessarily constant, represents the growth rate of mode n , and $k_n = 2\pi n/W$ is its spatial wave number. We take $k_n > 0$ without loss of generality. The magnitude of each perturbation mode is quantified by a dimensionless number ϵ_n , and $\epsilon_{n'} \neq \epsilon_n$ for any two modes n' and n in a mode-coupling analysis ([Miranda and Widom, 1998](#)). In the present work, we restrict ourselves to a single mode analysis, thus the sum may be dropped:

$$\zeta(y, t) = \zeta_0(t) + \epsilon a e^{iky + \lambda(t)}. \quad (7)$$

This approximation is justified since all mode coupling terms would be at least second order, or more specifically, coupling of modes n' and n would be of order $\epsilon_{n'} \epsilon_n$, which would be dropped eventually in our linear stability analysis below.

Next, we expand each phase's pressure p_j in perturbation series. Consistent with the interfacial perturbation in Eq. (7), only terms up to $\mathcal{O}(\epsilon)$ are kept:

$$p_j(x, y, t) = p_{0j}(x; t) + \epsilon p_{1j}(x, y; t), \quad (8)$$

where $p_{0j}(x; t)$ represents the base state, i.e., the pressure drop across the channel under uniform displacement. Meanwhile, $p_{1j}(x, y; t)$ is the pressure perturbation due to the interfacial disturbance. Note that the perturbative pressure expansion from Eq. (8) satisfies the steady PDE, i.e., Eq. (5), but may depend on time as a parameter due to the fluid–fluid interface's motion. Consistent with these definitions, the pressure gradient of the base state $p_{0j}(x; t)$ satisfies Darcy's equation and $p_{1j}(x, y; t)$ must vanish away from the interface, i.e., $\lim_{x \rightarrow -\infty} p_{11}(x, y; t) = \lim_{x \rightarrow +\infty} p_{12}(x, y; t) = 0$.

We proceed by expressing the pressure perturbation as a Fourier series:

$$p_{1j}(x, y; t) = \sum_n g_{jn}(x) e^{ik_n y + \lambda_n(t)}, \quad j = 1, 2, \quad (9)$$

where each $g_{jn} = \mathcal{O}(1)$. Again, Eq. (9) can be reduced to a single-mode representation due to higher-order terms being dropped in our linear stability analysis:

$$p_{1j}(x, y; t) = g_j(x) e^{iky + \lambda(t)}. \quad (10)$$

Solving the pressure equation by substituting Eqs. (8) and (10) into Eq. (5) (see Appendix for details), we obtain the pressure jump across the fluid–fluid interface:

$$\begin{aligned} (p_1 - p_2)|_{x=\zeta(y,t)} &= \frac{4U(\zeta_0(t))h_{in}}{\alpha[h(\zeta_0(t))]^2} (\mu_1 - \mu_2) \\ &+ \epsilon e^{iky + \lambda(t)} \frac{a\gamma Ca}{[h(\zeta_0(t))]^2} \left\{ (1 - M) - \left[\frac{\dot{\lambda}}{U(\zeta_0(t))} + \alpha \left(\frac{3}{h_{in}} - \frac{2}{h(\zeta_0(t))} \right) \right] \frac{1 + M}{k} \right\} + \mathcal{O}(\epsilon^2) \quad (\alpha \ll 1), \end{aligned} \quad (11)$$

where $Ca := 12U\mu_2/\gamma$ is the definition of the capillary number, γ is the interfacial surface tension as before, $M := \mu_1/\mu_2$ is defined as the ratio of the fluids' viscosities, and $U = U(\zeta_0(t))$ and $h = h(\zeta_0(t))$ are the

local (non-constant) velocity and depth at the unperturbed interface, respectively. It follows that Ca also depends on t , implicitly, through $U(\zeta_0(t))$ and $h(\zeta_0(t))$; however, we have left this dependency implicit to simplify the notation.

On the other hand, the capillary pressure jump at the interface $x = \zeta(y, t)$ also satisfies the Young–Laplace equation. If the defending fluid wets the wall, i.e., the contact angle between the defending fluid and the wall is $\theta_c = 0$, then Park and Homsy’s analysis (Park and Homsy, 1984) yields

$$(p_1 - p_2)|_{x=\zeta(y,t)} = \frac{2\gamma}{h[\zeta(y,t)]} \left(1 + 3.8Ca^{2/3} + \dots\right) + \frac{\gamma}{R} \left[\frac{\pi}{4} + \mathcal{O}(Ca^{2/3})\right], \quad (12)$$

where R is the radius of curvature of the interface, and we have taken into account the variable gap depth, $h[\zeta(y, t)] \neq \text{const.}$, as suggested by McCloud and Maher (1995). Neglecting higher-order terms (in this linear, $Ca \ll 1$ analysis), Eq. (12) simplifies to

$$(p_1 - p_2)|_{x=\zeta(y,t)} = \frac{2\gamma}{h[\zeta(y,t)]} + \frac{\pi}{4} \frac{\gamma}{R}. \quad (13)$$

If the wetting is not perfect, considering the contact angle θ_c , the pressure jump is written as

$$(p_1 - p_2)|_{z=\zeta(y,t)} = \gamma \left\{ \frac{2 \cos \theta_c}{h[\zeta(y,t)]} + f(\theta_c) \kappa \right\}, \quad (14)$$

where $\kappa = 1/R$ is the curvature of the interface, defined as

$$\begin{aligned} \kappa &:= -\frac{\partial^2 \zeta / \partial y^2}{[1 + (\partial \zeta / \partial y)^2]^{3/2}} \\ &= -\frac{\partial^2 \zeta}{\partial y^2} \left[1 - \frac{3}{2} \left(\frac{\partial \zeta}{\partial y} \right)^2 + \mathcal{O} \left(\left(\frac{\partial \zeta}{\partial y} \right)^4 \right) \right] \\ &= k^2 \epsilon a e^{iky + \lambda(t)} + \mathcal{O}(\epsilon^2), \end{aligned} \quad (15)$$

and $f(\theta_c)$ is a function of the contact angle to account for the interface curvature within the gap (Homsy, 1987, Park and Homsy, 1984). Specifically, based on the analysis of Lu et al. (2007),

$$f(\theta_c) = \left(\frac{\pi}{4} - \frac{\theta_c}{2} \right) \frac{1 + \sin \theta_c}{\cos \theta_c}. \quad (16)$$

Of course, this general expression yields the two standard cases: $f(0) = \pi/4$ and $f(\pi/2) = 1$ (interpreted as a limit).

Now, using the expansion in Eqs. (4) and (15), Eq. (14) becomes

$$(p_1 - p_2)|_{x=\zeta(y,t)} = \frac{2\gamma \cos \theta_c}{h(\zeta_0(t))} + \epsilon a \gamma e^{iky + \lambda(t)} \left\{ f(\theta_c) k^2 - \frac{2 \cos \theta_c \alpha}{[h(\zeta_0(t))]^2} \right\} + \mathcal{O}(\epsilon^2). \quad (17)$$

Matching the $\mathcal{O}(\epsilon)$ terms in Eqs. (11) and (17), we obtain

$$\begin{aligned} e^{iky + \lambda(t)} \frac{Ca \gamma a}{[h(\zeta_0(t))]^2} \left\{ (1 - M) - \left[\frac{\dot{\lambda}}{U(\zeta_0(t))} + \alpha \left(\frac{3}{h_{in}} - \frac{2}{h(\zeta_0(t))} \right) \right] \frac{1 + M}{k} \right\} = \\ \left\{ f(\theta_c) k^2 - \frac{2\alpha \cos \theta_c}{[h(\zeta_0(t))]^2} \right\} \gamma a e^{iky + \lambda(t)}. \end{aligned} \quad (18)$$

Rearranging the last equation, yields the *final form* of our theoretical prediction for the growth rate $\dot{\lambda}(t)$ of an interface between immiscible fluids in a rectilinear Hele-Shaw cell with a constant depth gradient α :

$$(1 + M) \left[\frac{\dot{\lambda}}{U(\zeta_0(t))} + \alpha \left(\frac{3}{h_{in}} - \frac{2}{h(\zeta_0(t))} \right) \right] = \left(1 - M + \frac{2\alpha \cos \theta_c}{Ca} \right) k - \frac{f(\theta_c) k^3 [h(\zeta_0(t))]^2}{Ca} \quad (\alpha \ll 1). \quad (19)$$

Equation (19) differs from the solution discussed by Al-Housseiny and Stone (2013) in that it does not assume an instantaneous development of the instability; rather the dynamics occurs over a finite time span during which the interface “sees” the cell’s depth variation. Thus, Eq. (19) captures the dynamic interplay between the growth/decay of a perturbation and the flow-wise geometric variations it encounters, as exemplified by $h(\zeta_0(t))$. Specifically, we have defined a non-constant $Ca = 12U\mu_2/\gamma$, where $U = U(\zeta_0(t))$ is *not* the fixed inlet value but, rather, it is the average velocity at some downstream cross-section $x = \zeta_0(t)$. $U = U(\zeta_0(t))$ can be easily determined by conservation of mass; see, e.g., the discussion of Eq. (24) below. Consequently, $\lambda(t)$ is governed by an *ordinary differential equation* (not an algebraic equation), and it may grow (or decay, or both) during its time evolution, despite the sign of $\dot{\lambda}$ obtained from a “frozen-time” linear stability analysis (Knobloch and Krechetnikov, 2015).

In the absence of a depth gradient, i.e., $\alpha = 0$ (thus, U and $Ca = \text{const.}$), Eq. (19) reduces to

$$\dot{\lambda} = \left(\frac{1-M}{1+M} \right) Uk - \frac{f(\theta_c)h_{in}^2 U}{Ca(1+M)} k^3, \quad (20)$$

which agrees exactly with the growth rate for the fingering instability given by Homsy (Homsy, 1987) for $\theta_c = \pi/2$, and if gravity and the Rayleigh–Darcy convection terms are neglected therein.

2.2 Classification of instability regimes

The threshold of instability is determined by setting $\dot{\lambda} = 0$. Then, from Eq. (19), we obtain

$$3\alpha(1+M) = \left(1 - M + \frac{2\alpha \cos \theta_c}{Ca} \right) h_{in} k - \frac{f(\theta_c)[h(\zeta_0(t))]^2 h_{in}}{Ca} k^3 \quad (\alpha \ll 1). \quad (21)$$

Solving for the *critical* capillary number, Ca_c , for fixed k in Eq. (21), we obtain

$$Ca_c = \frac{2\alpha \cos \theta_c - f(\theta_c)k^2[h(\zeta_0(t))]^2}{(1+M) \left(\frac{3}{h_{in}} - \frac{2}{h(\zeta_0(t))} \right) \frac{\alpha}{k} + (M-1)}. \quad (22)$$

This critical capillary number determines the threshold of instability for the fluid–fluid interface. The interface is stable if $Ca < Ca_c$; it is unstable if $Ca > Ca_c$. To the best of our knowledge, Eq. (22) is a new result because Ca_c implicitly depends on the interface location $x = \zeta_0(t)$ through $h(\zeta_0(t))$. Now, let us consider the possible flow and instability regimes in Hele-Shaw cells with a gap gradient by analyzing Eq. (22) in detail. Importantly, these flow regimes could not be determined (i.e., they do not exist) in previously analyses based on a fixed Ca_c .

Parallel cell. In this case, there is no depth gradient, i.e., $\alpha = 0$, and Eq. (22) becomes

$$Ca_c = -\frac{f(\theta_c)k^2 h_{in}^2}{(M-1)}. \quad (23)$$

The capillary number is constant along the cell, i.e., $Ca(x) \equiv Ca_{in} = Ca_{out}$. So, the critical capillary number delineates three regimes when compared with the inlet capillary number:

- **Regime I:** $Ca_{in} < Ca_c$. In this regime, the growth rate is negative, $\dot{\lambda} < 0$. The finger’s growth is suppressed, and the interface becomes flat asymptotically.
- **Regime II:** $Ca_{in} = Ca_c$. In this regime, the growth rate is zero, $\dot{\lambda} = 0$. The finger’s growth is neither inhibited nor triggered (i.e., this represents a marginally stable case). The finger’s length remains constant, and linear stability cannot determine whether an initial perturbation will grow or decay.
- **Regime III:** $Ca_{in} > Ca_c$. In this regime, the growth rate is positive, $\dot{\lambda} > 0$. The interface is unstable and the finger’s growth is triggered.

Diverging cell. In this case, $\alpha > 0$. The depth-averaged velocity of a stable flat interface is intrinsically a function of the channel's depth along the flow direction due to conservation of mass. This leads us to specifically decompose the capillary number into an inlet (constant) and local (variable) contribution:

$$Ca = \frac{12\mu_2 U}{\gamma} = Ca_{in} \frac{h_{in}}{h(\zeta_0)}, \quad (24)$$

where $Ca_{in} = 12\mu_2 U_{in}/\gamma$ and h_{in} are the constant capillary number and depth at the inlet of the cell. Ca as defined in Eq. (24) is implicitly a function of t through ζ_0 . This local Ca decreases with x because the velocity is decreasing for a diverging cell (expanding cross-sectional area). Although Ca_c decreases as well, according to Eq. (22), as $h(\zeta_0)$ increases, the change of the local Ca is faster than Ca_c . Therefore, we can still introduce three regimes by comparing the local Ca with Ca_c :

- **Regime I:** $Ca_{in} < Ca_c$. In this regime, the growth rate is always negative, $\dot{\lambda} < 0$, and the finger's growth is inhibited.
- **Regime II:** $Ca_{in} > Ca_c$ and $Ca_{out} < Ca_c$. In this regime, the growth rate is positive, $\dot{\lambda} > 0$, at the inlet, *but* changes sign becoming negative, $\dot{\lambda} < 0$, at some point downstream in the cell. Thus, the finger's length initially increases but then saturates and would be expected to decrease at longer times.
- **Regime III:** $Ca_{out} > Ca_c$. In this regime, the growth rate is always positive, $\dot{\lambda} > 0$, and the initial finger perturbation grows in time.

Converging cell. In this case, $\alpha < 0$. Now, local capillary number from Eq. (24) increases along the flow direction. Again, three instability regimes can be defined by comparing the local Ca with Ca_c :

- **Regime I:** $Ca_{out} < Ca_c$. In this regime, the growth rate is always negative, $\dot{\lambda} < 0$, and the finger's growth is inhibited.
- **Regime II:** $Ca_{in} < Ca_c < Ca_{out}$. In this regime, the growth rate is negative, $\dot{\lambda} < 0$, at the inlet, *but* changes sign becoming positive, $\dot{\lambda} > 0$, at some point downstream in the cell. The finger's length decreases initially but grows at longer times.
- **Regime III:** $Ca_{in} > Ca_c$. In this regime, the growth rate is always positive, $\dot{\lambda} > 0$, and the initial finger perturbation continues to grow in time.

It is important to note that this analysis predicts that, in diverging and converging cells, Regime II exists for a *finite* range of Ca_{in} values. This observation is in stark contrast to the parallel cells for which Regime II is simply the marginally stable case $Ca_{in} = Ca_c$. Thus, in diverging and converging Hele-Shaw cells, the stability of a perturbation may change during its evolution. Previous studies of elastic-walled Hele-Shaw cells also commented on this effect (Pihler-Puzović *et al.*, 2013, §4.2.1).

Now, to illustrate these three regimes for parallel, diverging and converging Hele-Shaw cells, in Fig. 2, we plot the growth rate $\dot{\lambda}$ as a function of the inlet capillary number Ca_{in} and the dimensionless flow-wise position $x^* = x/L$. The contact angle is assumed to be $\pi/2$, so we take $f(\theta_c) = 1$. In these plots, $x^* = 0$ and $x^* = 1$ represent the inlet and outlet, respectively. The intersection between a given $\dot{\lambda}$ surface and the horizontal plane $\dot{\lambda} = 0$ indicates a transition in (in)stability. Thus, our classification of instability into three regimes becomes clear. Regime I is to the left of the line of intersection, Regime III is to the right of this line, and Regime II refers to cases in which the line of intersection is crossed only for some range of Ca_{in} values. For example, in a parallel cell (Fig. 2a), the line of intersection is parallel to the x^* axis, thus Regime II corresponds to one specific value of Ca_{in} . For that value of Ca_{in} , the interface is neutrally stable. In a diverging cell (Fig. 2b) or a converging cell (Fig. 2c), on the other hand, the line of intersection is crossed for a *range* for Ca_{in} values, as one goes from the inlet to the outlet, i.e., from $x^* = 0$ to $x^* = 1$.

Furthermore, by comparing the growth rates in Figs. 2b and 2c, we observe that, for larger Ca_{in} , the growth rate in a converging cell could be greater than that in a diverging cell. This observation could explain the recent counterintuitive simulation results reported by (Jackson *et al.*, 2017), in which while the perturbation in a converging Hele-Shaw cell has a larger growth rate than in a parallel cell, the perturbation's growth rate in a diverging cell can be smaller, for large Ca_{in} , than in a parallel cell.

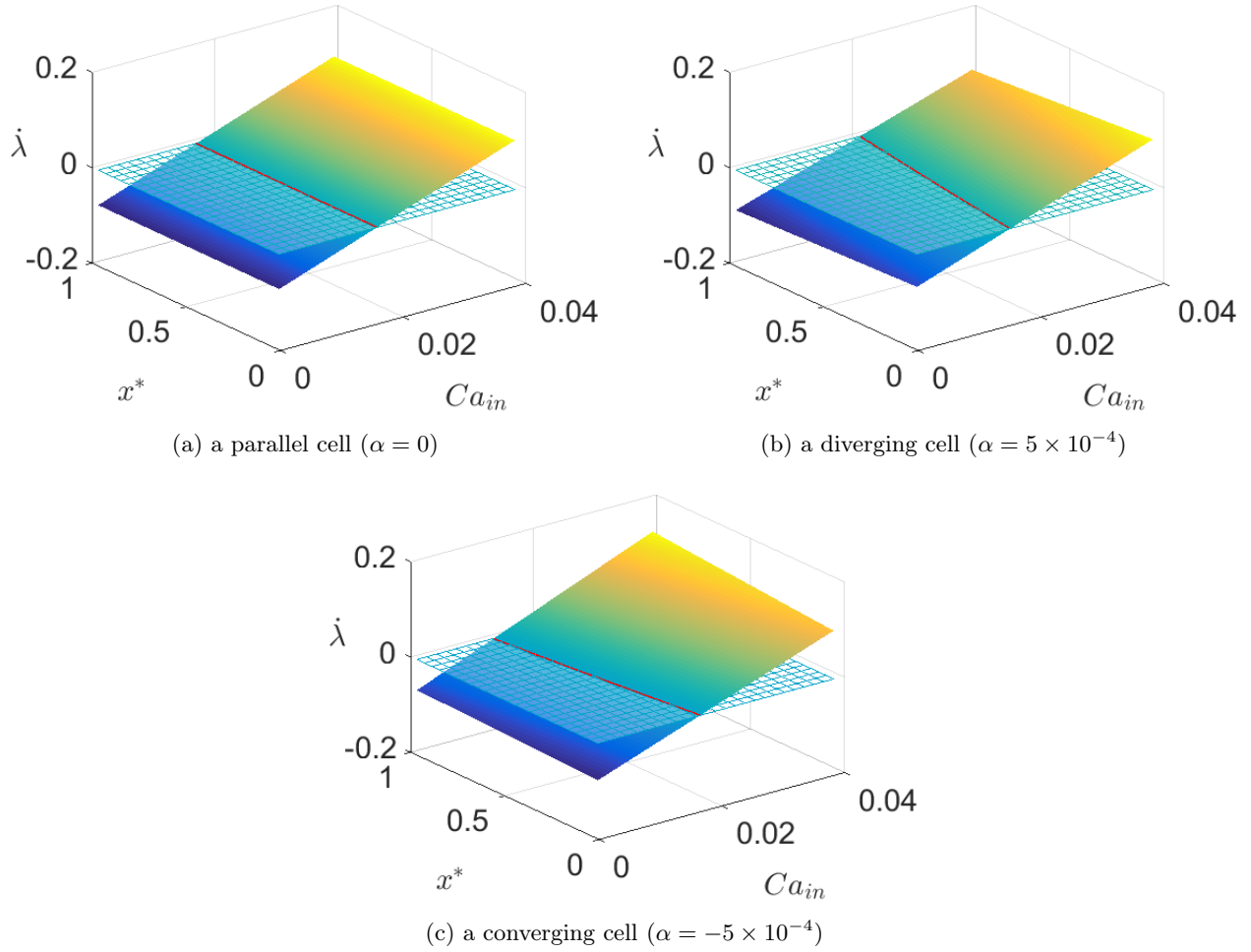


Figure 2: The growth rate $\dot{\lambda}$ as a function of inlet capillary number Ca_{in} and the flow-wise dimensionless position $x^* = x/L$ in different cells: (a) a parallel cell, (b) a diverging cell, and (c) a converging cell, with $M = 0.0154$ and other geometric/material properties as in Table 1. The intersection of the growth rate surface (shaded) and the $\dot{\lambda} = 0$ surface (meshed) is marked by red lines, indicating the change of sign of $\dot{\lambda}$ and an exchange of stability.

3 Direct numerical simulations

Numerical simulations are carried out using the interFoam solver (Damián, 2009, Deshpande et al., 2012) in OpenFOAM® ver. 6.0 (Weller et al., 1998), an open-source library based on the *finite volume method* (FVM) (Moukalled et al., 2016). In this analysis, the fluids are considered as incompressible, immiscible and unsteady. As depicted in Fig. 1, the fluids flow through a Hele-Shaw cell with a depth that varies with x . The contact angle between the displacing fluid and the wall is taken to be $\theta_c = \pi/2$ (the interface is flat across the depth). Three types of cells are considered: converging (negative depth gradient, $\alpha < 0$), parallel (zero gradient, $\alpha = 0$), and diverging (positive depth gradient, $\alpha > 0$).

Below, we present numerical “experiments” (studies) based on water (fluid 1) injected into mineral oil (fluid 2). The corresponding fluid properties, geometric parameters and flow quantities used for these simulations are summarized in Table 1. In simulations, the U_{in} values used are back-calculated from Ca_{in} .

Table 1: Fluid properties, geometric parameters and flow quantities used for the numerical simulations.

Property	Value (SI units)	Quantity	Value (SI units or –)
μ_1	1.0×10^{-3}	h_{in}	1×10^{-3}
ρ_1	1.0×10^3	W	5×10^{-2}
μ_2	6.50×10^{-2}	L	2×10^{-1}
ρ_2	8.30×10^2	α	$0, \pm 5 \times 10^{-4}, \pm 10 \times 10^{-4}$
γ	2.95×10^{-2}	Ca_{in}	0.0067 to 0.0200
θ_c	$\pi/2$		

3.1 Governing equations

In our DNS study, we solved the “full” 3D Navier–Stokes equation directly in each fluid, instead of the simplified and depth-averaged equations commonly solved in previous numerical studies. Specifically, the governing equations solved by the interFoam implementation (Deshpande et al., 2012) in OpenFOAM[®] are the conservation of mass and momentum for a *two-fluid mixture*, written as:

$$\nabla \cdot \mathbf{v} = 0, \quad (25)$$

$$\frac{\partial(\varrho \mathbf{v})}{\partial t} + \nabla \cdot (\varrho \mathbf{v} \otimes \mathbf{v}) = -\nabla p + \nabla \cdot [\eta(\nabla \mathbf{v} + \nabla \mathbf{v}^\top)] + \mathbf{F}, \quad (26)$$

where $\varrho = \varrho(x, y, z, t)$ is the mixture density, $\mathbf{v} = \mathbf{v}(x, y, z, t)$ is the mixture velocity, $p = p(x, y, z, t)$ is the pressure, $\eta = \eta(x, y, z, t)$ is the mixture viscosity, and \mathbf{F} is a fictitious body force used to enforce surface tension at the fluid–fluid interface. Physically, this body force due to surface tension results in a pressure jump at the interface, and it is evaluated (per unit volume) by the continuum surface force (CSF) model (Brackbill et al., 1992, Popinet, 2018):

$$\mathbf{F} = \gamma \kappa \nabla \phi, \quad (27)$$

where γ is the surface tension, and $\kappa = -\nabla \cdot (\nabla \phi / \|\nabla \phi\|)$ is the mean curvature of the fluid–fluid interface computed directly from its surface normals. Here, $\phi = \phi(x, y, z, t)$ is the phase fraction in a given cell of the computational grid, defined as

$$\phi \begin{cases} \in (0, 1) & \Rightarrow \text{Interface;} \\ = 1 & \Rightarrow \text{Fluid 1;} \\ = 0 & \Rightarrow \text{Fluid 2.} \end{cases} \quad (28)$$

The phase fraction keeps track of where each fluid (“1” and “2”) goes in the computational domain. We stress that this “mixture” model does not consider “different” physics than the mathematical model in Sect. 2; this is simply a numerical approach to handling dissimilar fluids separated by an immiscible interface.

In the interFoam solver, the phase fraction ϕ is solved using a modified volume-of-fluid (VOF) method (Hirt and Nichols, 1981):

$$\frac{\partial \phi}{\partial t} + \nabla \cdot (\phi \mathbf{v}) + \nabla \cdot (\phi(1 - \phi) \mathbf{v}_r) = 0, \quad (29)$$

where $\mathbf{v}_r = \mathbf{v}_1 - \mathbf{v}_2$ is the relative velocity between the two fluids. The fluid properties of the mixture, as well as the mixture velocity, to be used in Eqs. (25) and (26), can thus be expressed as

$$\varrho = \phi \rho_1 + (1 - \phi) \rho_2, \quad (30a)$$

$$\eta = \phi \mu_1 + (1 - \phi) \mu_2, \quad (30b)$$

$$\mathbf{v} = \phi \mathbf{v}_1 + (1 - \phi) \mathbf{v}_2, \quad (30c)$$

where the subscripts “1” and “2” refer to *fluid 1* (displacing) and *fluid 2* (displaced/defending), respectively. Eqs. (25), (26) and (29) are discretized spatially using the FVM and integrated in time via an Euler implicit scheme. Convection terms are discretized using a linear upwind scheme, while diffusion terms are discretized using a linear scheme. Gauss integration is employed for both terms, and gradients are corrected to account for non-orthogonal fluxes, which occur in angled cells. The Navier–Stokes solution algorithm used in

interFoam is “PIMPLE,” which is a combination of the *pressure-implicit with splitting of operators* (PISO) method (Issa, 1986, Ferziger and Perić, 2002) and the *semi-implicit method for pressure-linked equations* (SIMPLE) (Patankar and Spalding, 1972, Ferziger and Perić, 2002). In PIMPLE, PISO is used as the inner loop corrector to update pressure and velocity, and SIMPLE is used as the outer loop corrector to ensure convergence. Thus, PIMPLE achieves a more robust pressure-velocity coupling.

3.2 Mesh generation

When performing numerical simulations, on one hand, it is important to have a mesh that is fine enough to capture the physical properties accurately; on the other hand, a mesh with fewer cells saves computational resources. To balance accuracy and efficiency, we only refine the mesh in the region of interest, which in the present problem is the fluid–fluid interface. We use a relatively coarse mesh for the remainder of the Hele-Shaw cell. Since the interface is moving, adaptive mesh refinement is employed. At every time step the mesh is dynamically refined in the spatial region where $0.001 < \phi(x, y, z, t) < 0.999$, i.e., close to the interface to ensure it is well resolved. The initial mesh resolution is given in Table 2.

Table 2: Mesh generation for grid and time independence test(s) parameters for a parallel cell. For converging and diverging cells, only Δz changes.

Case ID	1	2	3
Grid elements	750	6,000	48,000
Grid resolution, Δx [m]	8×10^{-3}	4×10^{-3}	2×10^{-3}
Grid resolution, Δy [m]	5×10^{-3}	2.5×10^{-3}	1.25×10^{-3}
Grid resolution, Δz [m]	3.33×10^{-4}	1.67×10^{-4}	8.33×10^{-5}
Time step [s]	10^{-3}	10^{-4}	10^{-5}

3.3 Initial and boundary conditions

At the inlet ($x = 0$), we employ a horizontal velocity profile that satisfies no-slip at $z = 0, h_{in}$, i.e., $u_x(z) = -6U_{in}(z/h_{in} - 1/2)^2 + (3/2)U_{in}$, as the boundary condition for the mixture velocity. A zero-gradient boundary condition is employed for the flow at the outlet ($x = L$), except the pressure, which is fixed to zero to set the gauge. Initially, fluid 1 and fluid 2 are separated by a flat interface $x = \zeta_0 = 20$ mm. An initial perturbation is applied at the interface, i.e., $\zeta(y, 0) = \zeta_0[1 + \epsilon \sin(ky)]$ (see Fig. 3a). The initial magnitude of the perturbation is set by $\epsilon = 0.2$, and its wavenumber is $k = 2\pi/W$. Along the top ($z = h(x)$) and bottom ($z = 0$) plates of the cell, a no-slip boundary condition is prescribed. All variables are assumed to be periodic at the side (lateral) ends, $y = 0$ and $y = W$, of the cell. An example simulation under these initial and boundary conditions is shown in Fig. 3, highlighting how the initial perturbation can grow or decay, and how the interface remains sharp due to adaptive mesh refinement.

3.4 Grid and time step independence test

Three sets of simulations on different meshes, as listed in Table 2, were conducted to show grid and time step independence. We compute the deviation of the finger’s length, defined as $\xi(t) := \max_y[\zeta(y, t)] - \zeta_0(t)$, and found from linear stability analysis to be $\xi_{la}(t)$, to the simulation prediction $\xi_{ns}(t)$, as:

$$\varepsilon(t) = \left| \frac{\xi_{ns}(t) - \xi_{la}(t)}{\xi_{la}(t)} \right|. \quad (31)$$

The results in Fig. 4 show that the difference in the values of $\varepsilon(t)$ between case 2 and case 3 (less than 1%) is insignificant for the purposes of this study. Therefore, for the remainder of the present work, we will employ case 2 as the simulation grid of choice. This grid is less demanding in terms of computational resources than the grid from case 3.

4 Results: Comparing theory to simulations and stability regimes

4.1 Verification of the linear stability analysis

Hu *et al.* (2016) already performed extensive verification of the interFoam solver’s use for simulating viscous fingering in a Hele-Shaw cell of constant depth. Importantly, they showed that simulations can capture quite accurately experimental and theoretical predictions about the length and width of a *single* finger, as in the classical Saffman and Taylor (1958) experiments and analysis.

In this subsection, we explore flows in angled Hele-Shaw cells with different capillary numbers for converging ($\alpha < 0$), parallel ($\alpha = 0$) and diverging ($\alpha > 0$) cell geometries as cataloged by the ‘cases’ in Table 3. We wish to verify the linear stability theory from Sec. 2 through numerical simulations. Before we discuss the numerical results in detail, it is instructive to make a few remarks. First, the linear analysis holds, strictly speaking, only at the moment of initiation (onset) of instability. Nevertheless, the linear analysis is generally used in the literature to describe the unstable interface’s evolution. Additionally, here for simplicity and for consistency with some previous analyses, only one Fourier mode was used to represent the perturbation. At later times in the displacement process, the simulations capture the full nonlinear unstable interface evolution, which is expected to be qualitatively similar (but quantitatively different) than the prediction of the linear analysis. This specific point is of interest to us in the present work. Even when linear theory does not provide precise quantitative prediction about the interface’s evolution (and, instead, direct numerical simulations must be used), linear theory correctly delineates the stability regimes and their transitions in the capillary number–depth gradient, i.e., (Ca, α) , space.

The first verification results are presented in Fig. 5 for each of the three types of Hele-Shaw cells in panels (a), (b) and (c). Solid and dotted lines refer to numerical and theoretical results, respectively. Lines with different symbols represent different cases from Table 3 with different inlet capillary numbers Ca_{in} . The finger’s length ξ (left panels) and growth rate $\dot{\lambda}(t)$ (right panels) are plotted as functions of time. The theoretical predictions are computed from Eqs. (6) and (19) with $\xi(t) = \max_y[\zeta(y, t)] - \zeta_0(t)$. Numerical results are post-processed from the simulation data; the finger’s length is calculated as $\xi(t) = \{\max_y[\zeta(y, t)] + \min_y[\zeta(y, t)]\}/2$, and the growth rate is calculated as $\dot{\lambda}(t) = [1/\xi(t)]d\xi/dt$ using the cubic-spline interpolation with smoothing available in SciPy (Jones *et al.*, 2001).

Table 3: Classification of cases for simulations used for verification of the linear theory.

	$Ca_{in} = 0.0067$	$Ca_{in} = 0.0147$	$Ca_{in} = 0.0200$
Converging cell ($\alpha = -5 \times 10^{-4}$)	Case 4	Case 5	Case 6
Parallel cell ($\alpha = 0$)	Case 7	Case 8	Case 9
Diverging cell ($\alpha = 5 \times 10^{-4}$)	Case 10	Case 11	Case 12

Numerical results and linear stability analysis agree very well at $Ca_{in} = 0.0200$ in each cell: Case 6 in Fig. 5a; Case 9 in Fig. 5b; and Case 12 in Fig. 5c. In these cases, the finger’s length $\xi(t)$ increases over time and the growth rate $\dot{\lambda}(t)$ remains positive, meaning that the interface is unstable, which corresponds to Regime III in classification introduced in Sec. 2. At $Ca_{in} = 0.00147$, numerical simulations show a roughly constant finger’s length. The growth rate is almost zero (Case 8 in Fig. 5b), or suffers a change of sign (Case 5 in Fig. 5a and Case 11 in Fig. 5c). At this value of Ca_{in} we are reminded of Regime II from the linear stability analysis. As Ca_{in} is decreased to 0.0067, simulations show that $\xi(t)$ continues to decay, and $\dot{\lambda}(t)$ is always negative: Case 4 in Fig. 5a; Case 7 in Fig. 5b; and Case 10 in Fig. 5c.

Therefore, the prediction from linear stability theory regarding three instability regimes has been verified through numerical simulations. However, the quantitative prediction of the growth rate from linear analysis is most accurate in Regime III, which corresponds to the classical Saffman–Taylor instability. In Regime I and II, our results quantify the difference between the linear model and 3D DNS. Indeed, as the interface becomes flattened, it is increasingly less meaningful to try to define the finger’s length as the difference between maximum and minimum extent. In this case, integrated metrics such as the isoperimetric ratio have been preferred by other authors (Morrow *et al.*, 2019). Moreover, we have verified that the evolution of the perturbations according to linear stability theory and DNS match more closely (quantitatively) for smaller

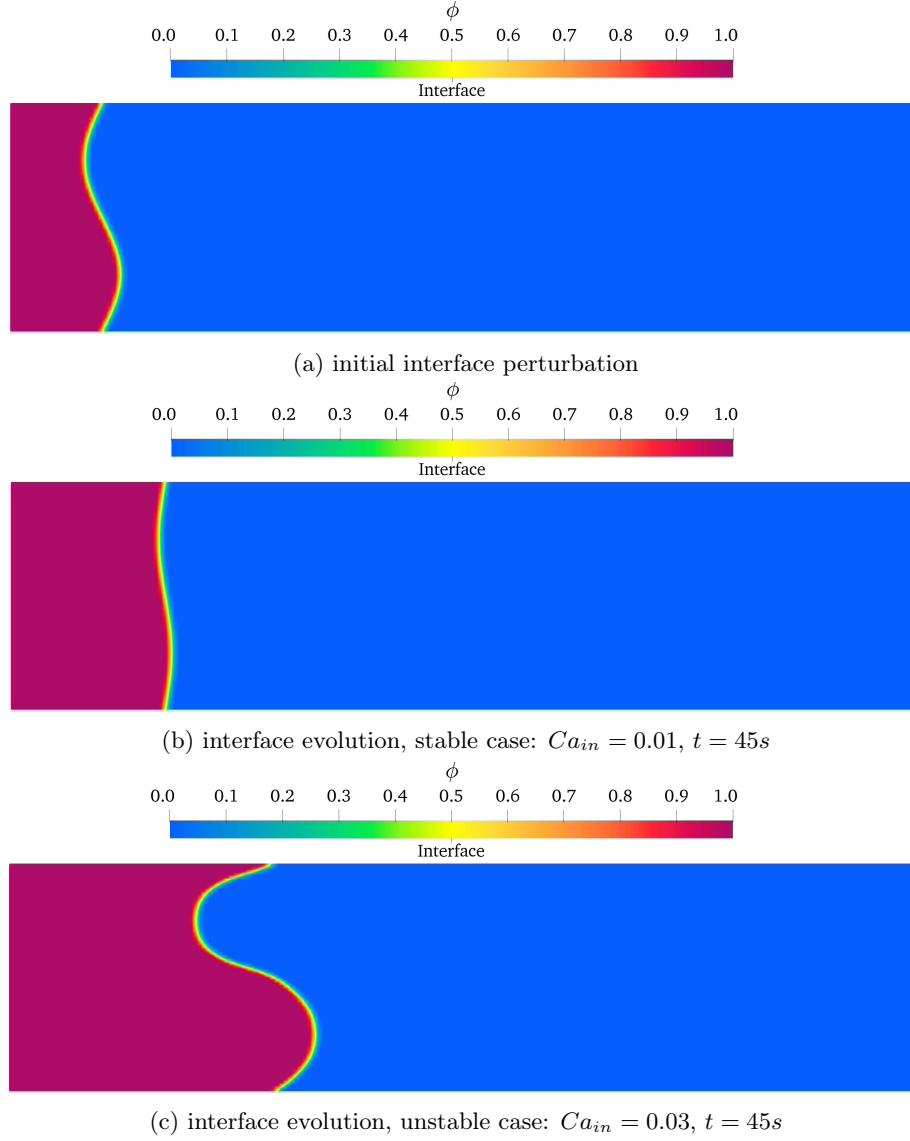


Figure 3: Top view of example simulation of interface evolution in a converging cell ($\alpha = -5 \times 10^{-4}$).

perturbation magnitudes, e.g., taking $\epsilon = 0.05$ or even 0.02 . However, to better resolve these very small (and slower growing perturbations), a finer mesh should be used. The effect of the perturbation magnitude ϵ is not an emphasis of the present study, hence these details are omitted for brevity. As mentioned earlier, we use the small but not infinitesimal value of $\epsilon = 0.2$ in all of our DNS results.

4.2 The effect of the flow-wise depth gradient

In this subsection, we investigate the effect of the depth gradient α on the growth/decay of perturbations on the fluid–fluid interface. The various cases with different values of α are cataloged in Table 4. The theoretical predictions and numerical results for the growth rate $\lambda(t)$, as defined in Sec. 2, in these different (in)stability regimes are shown in Figs. 6a, 6c and 6e, respectively, for different values of α . The results show that as α increases, λ decreases. In other words, following the terminology most recently used in (Anjos *et al.*, 2018a), the diverging cells have a relatively stabilizing effect in all three regimes, while converging cells relatively destabilize the interface, compared to the interface evolution in a parallel cell for the same value of Ca_{in} . Specifically, the growth rate from 3D simulations is not constant, but varies with time, which

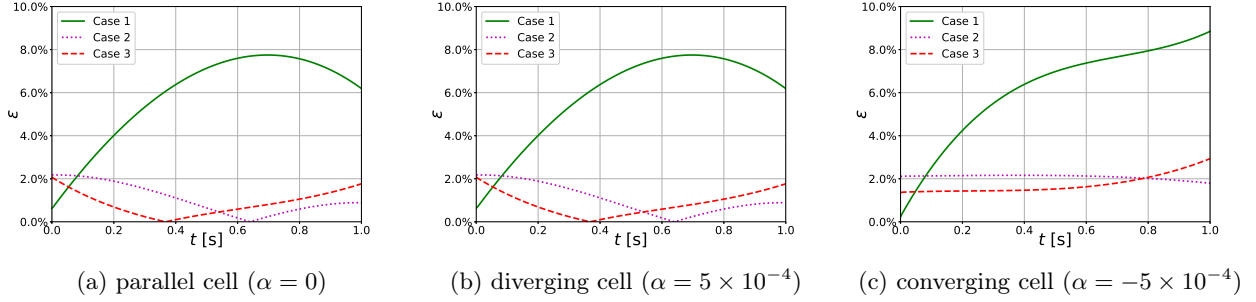


Figure 4: Grid and time step independence tests show the % difference in the fingers length (between linear stability and numerical simulation) as a function of time. Clearly, the simulation parameters in case 2 and case 3 lead to very similar results, so case 2 shall be employed for all simulations herein.

Table 4: Classification of the simulations conducted to ascertain the effect of the depth gradient.

	Regime I $Ca_{in} = 0.0067$	Regime II $Ca_{in} = 0.0147$	Regime III $Ca_{in} = 0.0200$
$\alpha = -10 \times 10^{-4}$	Case 13	Case 14	Case 15
$\alpha = -5 \times 10^{-4}$	Case 4	Case 5	Case 6
$\alpha = 0$	Case 7	Case 8	Case 9
$\alpha = 5 \times 10^{-4}$	Case 10	Case 11	Case 12
$\alpha = 10 \times 10^{-4}$	Case 16	Case 17	Case 18

qualitatively verifies our novel extension of previous linear stability analysis (Sec. 2).

To further compare the effect of the depth gradient in each regime, in Fig. 6b, 6d and 6f, we present the integral of growth rate over time, i.e., $\lambda(t) = \int_0^t \dot{\lambda}(t') dt' = \int_{\xi(0)}^{\xi(t)} d\xi'/\xi' = \ln|\xi(t)| - \ln|\xi(0)|$, which is computed over the first 20 s of simulation time. In Regime I (see Fig. 6 top row), the simulation results show that the depth gradient has a slight effect on the interface: the integral of the growth rate λ decreases slightly with α . The present linear stability analysis exaggerates the gradient's effect: the predicted slope of λ , as a function of α , is larger than the one from DNS. We conjecture that a weakly-nonlinear stability analysis (e.g., extending the work of (Miranda and Widom, 1998) to the case of an angled Hele-Shaw cell), which keeps higher-order terms in the perturbation expansion, could correct this exaggeration. Moreover, since λ is decreasing and negative, then the suppression of viscous fingering that exists in Regime I is most effective in *diverging* cells, and the larger α , the better. This result is somewhat counterintuitive compared to discussion in (Al-Housseiny et al., 2012) wherein converging cells are described as the most stabilizing; however, in (Al-Housseiny et al., 2012) the three regime diagram proposed herein was obviously not considered.

In Regime II (see Fig. 6 middle row), the effect of the gradient is stronger than in Regime I: as α increases, λ decreases more rapidly. The gap gradient has the most significant effect in Regime III (see Fig. 6 bottom row), indicating that the triggering of fingering in Regime III is most clearly observed in converging cells, and the larger $|\alpha|$, the better. Returning to the comparison with the previous linear stability analysis from (Al-Housseiny et al., 2012) (dotted lines with stars in Fig. 6b, 6d and 6f), we observe that it does not capture the decreasing trend of λ with α , specifically because in our simulations we have taken a contact angle of $\theta_c = \pi/2$.

In general, the linear stability analysis provides a theoretical explanation for the DNS results, specifically in the prediction of the dependence of the growth rate on the depth gradient α in an angled Hele-Shaw cell (Fig. 6b, 6d and 6f). As the capillary number decreases, the discrepancy between theory and simulation increases, as is to be expected for this $Ca \ll 1$ linear theory. In particular, one way to understand this observation is to note that as Ca_{in} decreases, the interface becomes more and more flattened, and the finger's length is no longer a sensitive metric.

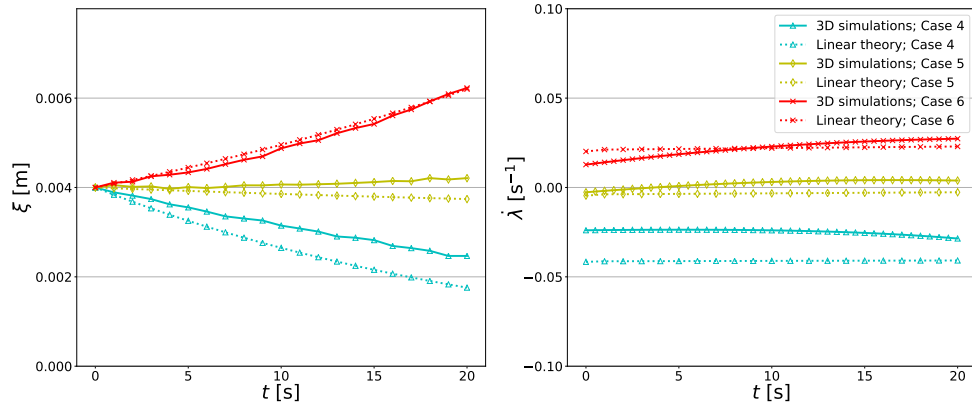
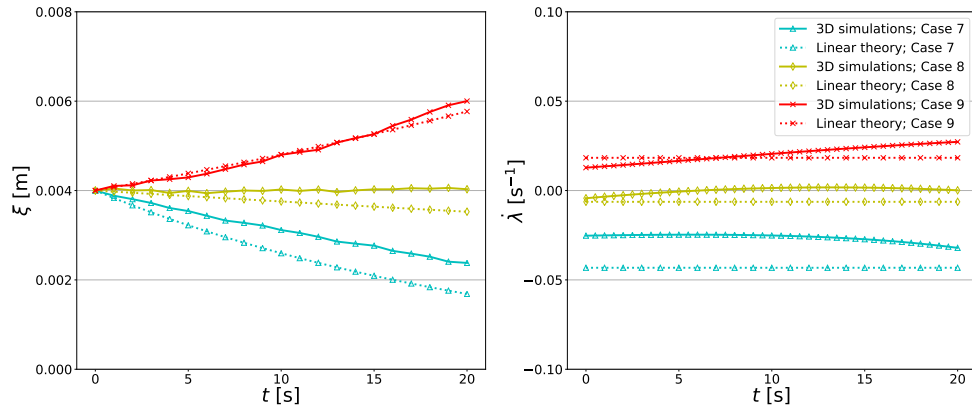
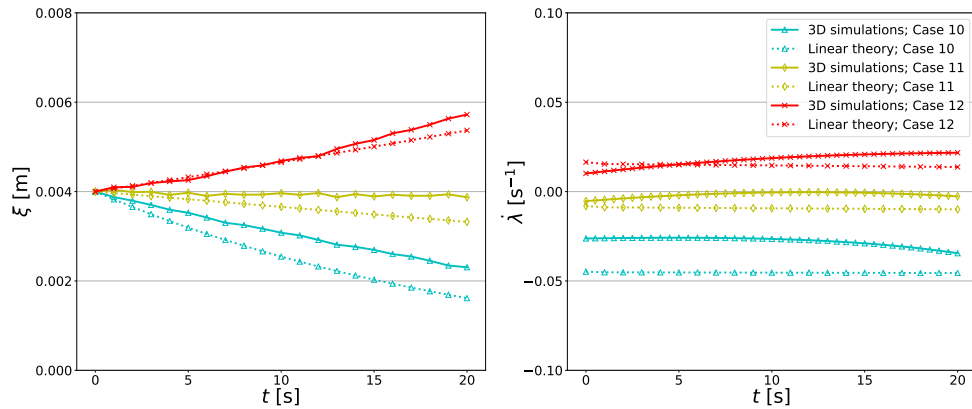
(a) a converging cell with $\alpha = -5 \times 10^{-4}$ (b) a parallel cell with $\alpha = 0$ (c) a diverging cell with $\alpha = 5 \times 10^{-4}$

Figure 5: Linear stability analysis verification for the finger's length $\xi(t)$ and the growth rate $\dot{\lambda}(t)$ in (a) a converging cell (Cases 4, 5, 6), (b) a parallel cell (Cases 7, 8, 9), (c) a diverging cell (Cases 10, 11, 12). Colors represent different inlet Ca , as labelled. Simulations results (solid curves) verify the three regimes theory: blue solid curves (decreasing ξ and $\dot{\lambda} < 0$) are in Regime I, yellow solid curves (roughly constant ξ and $\dot{\lambda} \approx 0$) are in Regime II, and red solid curves (increasing ξ and $\dot{\lambda} > 0$) are in Regime III.

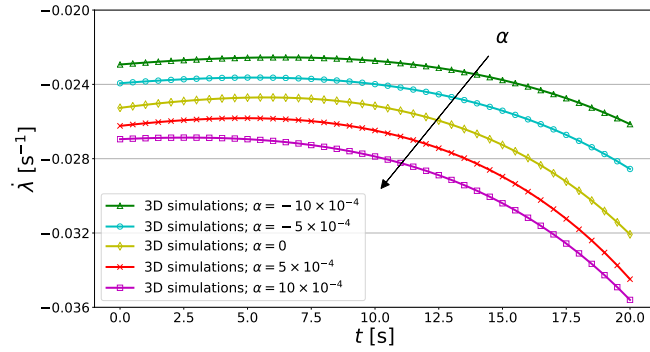
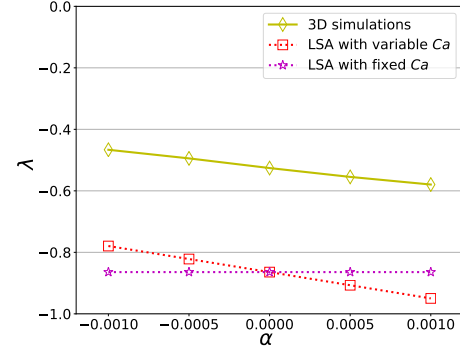
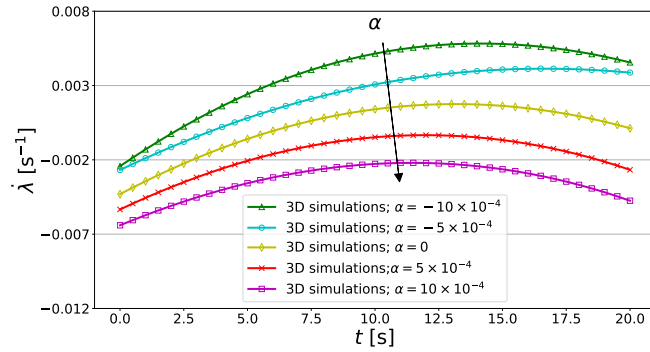
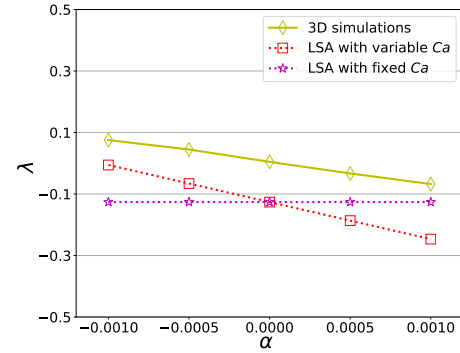
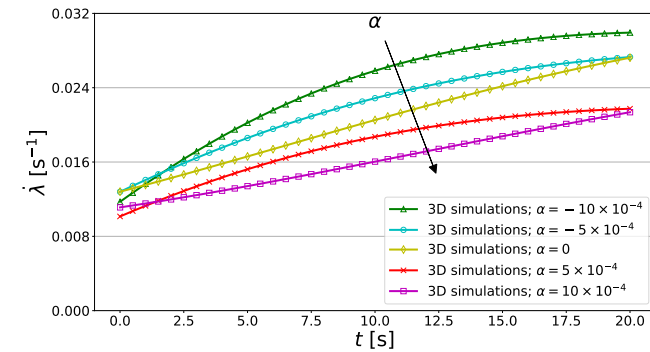
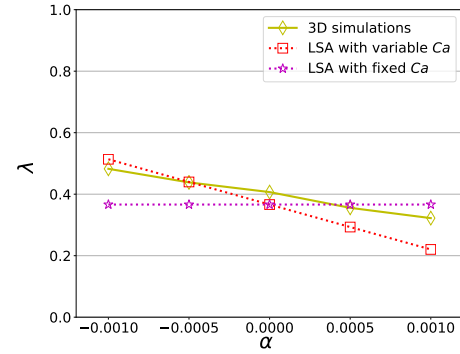
(a) Regime I ($Ca = 0.0067$)(b) Regime I ($Ca = 0.0067$)(c) Regime II ($Ca = 0.0147$)(d) Regime II ($Ca = 0.0147$)(e) Regime III ($Ca = 0.0200$)(f) Regime III ($Ca = 0.0200$)

Figure 6: The effect of depth gradient α on the growth rate $\dot{\lambda}(t)$ (a,c,e) and the integral of the growth rate λ (b,d,f), in the three regimes. As α increases, $\dot{\lambda}$ decreases. The growth rate from 3D simulations is not constant but varies with time, which qualitatively verifies our linear stability analysis from Sec. 2, denoted as “LSA with variable Ca .” “LSA with fixed Ca ” stands for the quasi-steady analysis of Al-Housseiny *et al.* (2012). LSA with fixed Ca does not capture the decreasing trend of λ with α obtained by the present LSA with variable Ca and 3D DNS. In turn, the latter exaggerates the gradient’s effect compared to DNS.

4.3 Stability diagram

In Sec. 4.1, the linear analysis was verified through numerical simulations of flows throughout the three regimes of the proposed stability classification. However, for marginal cases near the dividing curves between two regimes, we observed that the predictions of the linear theory do not quantitatively agree with DNS. To better understand this discrepancy, we conducted further numerical experiments to explore the numerical regime map for various depth gradient values α . In this subsection, we compare the numerical regime diagram to the theoretically predicted one. The result is shown in Fig. 7. Other stability diagrams from previous research (Bongrand and Tsai, 2018, Kim *et al.*, 2017, Brandão *et al.*, 2018) have shown the (in)stability by linear stability analysis, experiments, or both. Here, we supplement the diagram with 3D direct numerical simulation results, and make a comparison with the linear stability analysis.

The theoretical division of (in)stability regimes in a Hele-Shaw cell is based on the local capillary number at the inlet, Ca_{in} . The critical capillary number Ca_c for a particular angled Hele-Shaw cell is obtained from Eq. (22). By setting $Ca_{in} = Ca_c$ or $Ca_{out} = Ca_c$, we obtain the Ca_{in} and Ca_{out} values at the onset of the stability transition, respectively. Then, we refer both critical cases back to Ca_{in} , by computing the corresponding value of Ca_{in} for $Ca_{out} = Ca_c$. Thus, we obtain two sets of Ca_{in} values, computed from setting $Ca_{in} = Ca_c$ and from $Ca_{out} = Ca_c$, respectively, which divide the flow into three regimes in the (α, Ca_{in}) plane. Note that the stability diagram depends on the Hele-Shaw cell's geometry because the Ca_{in} that we compute from $Ca_{out} = Ca_c$ is related to the length of the channel. However, in our simulation the interface never reaches the end of the Hele-Shaw cell. Therefore, the horizontal length scale to be used in the nondimensionalization should be reconsidered to determine whether the interface will change its stability during its transit of the initial length of the Hele-Shaw cell. To make a reasonable comparison with the simulation results, we evaluate Ca_{out} at $x = 40$ mm, the maximum distance reached by the interfaces in the simulations.

The theoretically predicted regime divisions are shown in Fig. 7 as dashed curves. The Ca_{in} values calculated from $Ca_{in} = Ca_c$ are plotted with circles, while the ones obtained from $Ca_{local} = Ca_c$ are plotted with crosses. Note that there is an intersection between the two curves at $\alpha = 0$ because in this case there is no sense in which to distinguish Ca_{in} from Ca_{local} . For $\alpha \neq 0$, the local capillary number at the inlet Ca_{in} is the minimum capillary number in converging cells ($\alpha < 0$), while it is the maximum capillary number in diverging cells ($\alpha > 0$). Therefore, the critical Ca_{in} from $Ca_{in} = Ca_c$ separates Regime II from Regime III in converging cells, while it separates Regime I from Regime II in diverging cells. The intersection could also be interpreted as follows: as $|\alpha|$ decreases, the range of Regime II narrows, finally collapsing to a point for $\alpha = 0$ (parallel cell, i.e., the “classical” Saffman–Taylor case).

Solid curves are the results of direct numerical simulations, representing the division of the parameter space into three regimes as predicted by the 3D evolution of the interface. Numerical experiments were carried out for $\alpha = 0, \pm 5 \times 10^{-4}$ and $\pm 10 \times 10^{-4}$, across multiple Ca_{in} values ranging from 0.0067 to 0.02 with a step of 0.0013. The numerical results show a general agreement with the theoretically predicted regime map, except for Regime II. This is not surprising because the marginally stable regime is hard to capture in simulations.

The stability diagram in Fig. 7 also captures the effect of depth gradient on the regimes: as α increase, the regimes boundaries move up to larger Ca_{in} values. In particular, we observe that simulations predict a much weaker dependence on α than the linear stability analysis.

5 Conclusions

In this work, we analyzed the instability of the interface between immiscible viscous fluids in angled Hele-Shaw cells with small constant depth gradient in the flow-wise direction. We performed a linear stability analysis, and we derived an analytical solution for the time-dependent (not constant) growth rate $\dot{\lambda}(t)$ of perturbations to a flat interface. Our theoretical result takes into account the geometric variations and the local capillary number Ca due to the changing cross-sectional area of the flow conduit. Specifically, we have analyzed the case, not previously considered, of the interface instability developing on a time scale on which the flow-wise geometric variations matter. Consequently, dynamic changes in stability were shown to be possible during the interface's propagation. Then, we obtained a critical capillary number Ca_c by letting $\dot{\lambda} = 0$. By comparing the local capillary number with Ca_c , we put forward a division of the stability diagram

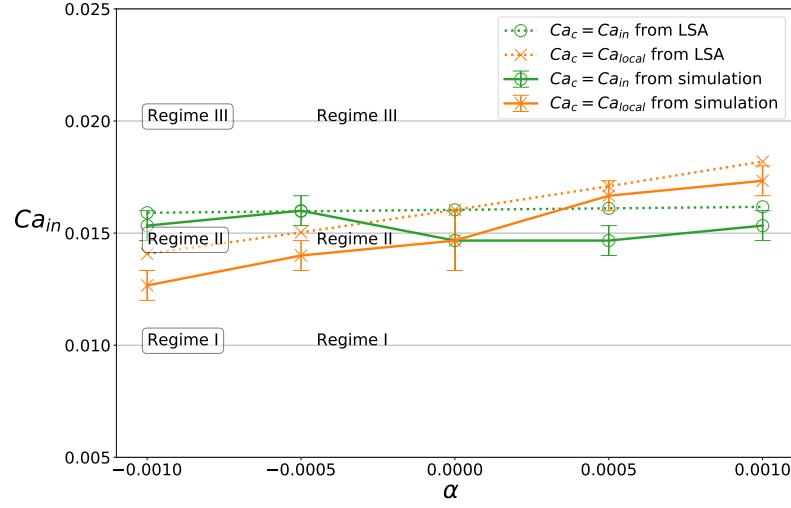


Figure 7: Stability Diagram: theoretical and numerical results are plotted as dashed and solid curves, respectively. Green and orange curves represent the critical situations such that $Ca_c = Ca_{in}$ and $Ca_c = Ca_{local}$, respectively. The error bars represent the difference in Ca_{in} between two simulations. The boxed regimes are those defined by the linear theory and the others are those defined via direct numerical simulations.

into three regimes. In Regime I, the interface is always stable; in Regime II, the interface remains neutrally stable (in a parallel cell), while in angled cells, an exchange of stability occurs at a specific position in the cell: from stable to unstable (in a converging cell), or from unstable to stable (in a diverging cell). This regime classification implies, in particular, that whether or not a depth gradient is stabilizing (or destabilizing) for a given inlet flow rate (thus, given capillary number) depends on which regime the flow falls into. Therefore, a negative depth gradient (converging geometry) is not generically a stabilizing mechanism.

Next, we performed 3D direct numerical simulations of the same physical system, using the interFoam solver built onto the OpenFOAM® platform, in order to verify the proposed three regimes theory. In Regime III, the finger's length and growth rate computed from simulations agree well with theoretical predictions, verifying the linear stability analysis for the classical Saffman–Taylor instability. Meanwhile, in Regimes I and II, the simulation results support the regimes' existence, but do not match the λ values predicted by linear stability, due to the former's limitations discussed above.

More importantly, however, the proposed linear theory, when compared to the simulation results, correctly captures the general dependence of the interface growth rate on the depth gradient. Specifically, in Regime I, simulation results show that the integral of the growth rate λ decreases slightly with the gap gradient; meanwhile, linear stability analysis exaggerates the effect, which is expected to be corrected by employing a weakly-nonlinear stability analysis. Simulations also suggest that the suppression of fingering in Regime I is most robust in diverging angled Hele-Shaw cells. Furthermore, in Regime II, the effect of the gradient is stronger than that in Regime I. The gap gradient's effect is significant in Regime III, in which case it acts to trigger the fingering instability, especially in converging cells. In all three regimes, the diverging (converging) cells have a relatively stabilizing (destabilizing) effect, with respect to the interface evolution in parallel cells for the same Ca value, which is contrary to the intuition developed in recent experimental studies.

Finally, we compared the regime stability diagram in the (α, Ca_{in}) plane as predicted by theory and as computed from simulations. Although there are some expected systematic sources of error between theory and simulation here, the stability diagram in Fig. 7, to the best of our knowledge, for the first time, compares 3D direct numerical simulations with linear stability analysis of instability in an angled Hele-Shaw cell. Consequently, the present work might provide a framework through which to understand interfacial (in)stability in the presence of geometry variations. Specifically, researchers may:

1. compare quantitatively their simulation or experimental results against the stability diagram (Fig. 7) to

determine in which regime applies, and therefore understand whether the depth gradient is stabilizing or destabilizing;

2. solve the ordinary differential equation (19) for the growth of the interface under the specific flow and geometric conditions of their simulation or experiment, to determine the expected behavior of perturbations of the fluid–fluid interface (growth, decay, or *both*).

Additionally, we hope that this stability diagram provides a methodology for addressing the question of how one might improve the sweep efficiency of fluid–fluid displacements in complex fractured rock composed of a network of non-uniform passages. For example, if the flow (for a particular diverging or converging flow passage) can be controlled and forced into Regime I, or at least into Regime II, the interfacial instabilities can be mitigated. Such fundamental understanding of fingering control can also be employed to minimize the risk of geomechanical phenomena during overflushing. In fact, it was shown (Osipov *et al.*, 2018) that viscous fingering (occurring in Regime III) causes a non-uniform sweep of proppants in a fracture, which are important to distribute uniformly to prevent the fracture’s collapse.

Future work should consider a weakly-nonlinear analysis with mode coupling to extend the predictive capability of the stability theory. Furthermore, direct numerical simulation could be employed to verify studies on the critical wave number k_c at fixed Ca , such as the prior work of Miranda and Widom (1998). In fact, simulations possess a crucial advantage over experiments: simulations allow precise control over the initial conditions, including the wave number of the interfacial disturbance. Finally, the effects of shear-dependent viscosity (Wang *et al.*, 2019), yield stress (Borodin *et al.*, 2015) and viscoelasticity (Malhotra and Sharma, 2014) on the interfacial instability in angled Hele-Shaw cells should be investigated, building upon the previous work in parallel cells. This aspect of future work is particularly relevant given that non-Newtonian fluids are commonly used in hydraulic fracturing applications (Barbati *et al.*, 2016, Osipov, 2017).

Acknowledgements

Acknowledgment is made to the donors of the American Chemical Society Petroleum Research Fund for support of this research under ACS PRF award # 57371-DNI9. I.C.C. would like to thank T. T. Al-Housseiny for many enlightening discussions on control of interfacial instabilities over the years. We thank Michael Jackson (Queensland University of Technology) for pointing out a missing term in an earlier version of the expression for the growth rate.

References

- Al-Housseiny TT, Stone HA (2013) Controlling viscous fingering in tapered Hele-Shaw cells. *Phys Fluids* 25:092102, DOI 10.1063/1.4819317
- Al-Housseiny TT, Tsai PA, Stone HA (2012) Control of interfacial instabilities using flow geometry. *Nat Phys* 8:747–750, DOI 10.1038/nphys2396
- Al-Housseiny TT, Christov IC, Stone HA (2013) Two-phase fluid displacement and interfacial instabilities under elastic membranes. *Phys Rev Lett* 111:034502, DOI 10.1103/PhysRevLett.111.034502
- Alvarez-Lacalle E, Pauné E, Casademunt J, Ortín J (2003) Systematic weakly nonlinear analysis of radial viscous fingering. *Phys Rev E* 68:026308, DOI 10.1103/PhysRevE.68.026308
- Anjos PHA, Dias EO, Miranda JA (2017) Radial fingering under arbitrary viscosity and density ratios. *Phys Rev Fluids* 2:084004, DOI 10.1103/PhysRevFluids.2.084004
- Anjos PHA, Dias EO, Miranda JA (2018a) Fingering instability transition in radially tapered Hele-Shaw cells: Insights at the onset of nonlinear effects. *Phys Rev Fluids* 3:124004, DOI 10.1103/PhysRevFluids.3.124004
- Anjos PHA, Lira SA, Miranda JA (2018b) Fingering patterns in magnetic fluids: Perturbative solutions and the stability of exact stationary shapes. *Phys Rev Fluids* 3:044002, DOI 10.1103/PhysRevFluids.3.044002

- Anna SL (2016) Droplets and bubbles in microfluidic devices. *Annu Rev Fluid Mech* 48:285–309, DOI 10.1146/annurev-fluid-122414-034425
- Barbati AC, Desroches J, Robisson A, McKinley GH (2016) Complex fluids and hydraulic fracturing. *Annu Rev Chem Biomol Eng* 7:415–453, DOI 10.1146/annurev-chembioeng-080615-033630
- Basaran OA, Gao H, Bhat PP (2013) Nonstandard Inkjets. *Annu Rev Fluid Mech* 45:85–113, DOI 10.1146/annurev-fluid-120710-101148
- Bear J (1972) *Dynamics of Fluids in Porous Media*. Environmental Science, American Elsevier Publishing Company, Inc., New York, NY
- Bongrand G, Tsai PA (2018) Manipulation of viscous fingering in a radially tapered cell geometry. *Phys Rev E* 97:061101, DOI 10.1103/PhysRevE.97.061101
- Boronin SA, Osipov AA, Desroches J (2015) Displacement of yield-stress fluids in a fracture. *Int J Multiphase Flow* 76:47–63, DOI 10.1016/j.ijmultiphaseflow.2015.07.001
- Brackbill JU, Kothe DB, Zemach C (1992) A continuum method for modeling surface tension. *J Comput Phys* 100:335–354, DOI 10.1016/0021-9991(92)90240-Y
- Brandão R, Dias EO, Miranda JA (2018) Immiscible three-dimensional fingering in porous media: A weakly nonlinear analysis. *Phys Rev Fluids* 3:034002, DOI 10.1103/PhysRevFluids.3.034002
- Carrillo L, Magdaleno FX, Casademunt J, Ortín J (1996) Experiments in a rotating Hele-Shaw cell. *Phys Rev E* 54:6260–6267, DOI 10.1103/PhysRevE.54.6260
- Chen X, Hopkins BJ, Helal A, Fan FY, Smith KC, Li Z, Slocum AH, McKinley GH, Carter WC, Chiang YM (2016) A low-dissipation, pumpless, gravity-induced flow battery. *Energy Environ Sci* 9:1760–1770, DOI 10.1039/C6EE00874G
- Chuoque RL, van Meurs P, van der Poel C (1959) The instability of slow, immiscible, viscous liquid-liquid displacements in permeable media. *Petroleum Transactions, AIME* 216:188–194, DOI SPE-1141-G
- Damián SM (2009) Description and utilization of interFoam multiphase solver. Tech. rep., International Center for Computational Methods in Engineering, URL <http://infofich.unl.edu.ar/upload/3be0e16065026527477b4b948c4caa7523c8ea52.pdf>
- Deshpande SS, Anumolu L, Trujillo MF (2012) Evaluating the performance of the two-phase flow solver interFoam. *Comput Sci Disc* 5:014016, DOI 10.1088/1749-4699/5/1/014016
- Dias EO, Miranda JA (2010a) Control of radial fingering patterns: A weakly nonlinear approach. *Phys Rev E* 81:016312, DOI 10.1103/PhysRevE.81.016312
- Dias EO, Miranda JA (2010b) Finger tip behavior in small gap gradient Hele-Shaw flows. *Phys Rev E* 82:056319, DOI 10.1103/PhysRevE.82.056319
- Dias EO, Miranda JA (2013) Taper-induced control of viscous fingering in variable-gap Hele-Shaw flows. *Phys Rev E* 87:053015, DOI 10.1103/PhysRevE.87.053015
- Dias EO, Parisio F, Miranda JA (2010) Suppression of viscous fluid fingering: A piecewise-constant injection process. *Phys Rev E* 82:067301, DOI 10.1103/PhysRevE.82.067301
- Dias EO, Alvarez-Lacalle E, Carvalho MS, Miranda JA (2012) Minimization of viscous fluid fingering: A variational scheme for optimal flow rates. *Phys Rev Lett* 109:144502, DOI 10.1103/PhysRevLett.109.144502
- Díaz-Piola L, Planet R, Campàs O, Casademunt J, Ortín J (2017) Fluid front morphologies in gap-modulated Hele-Shaw cells. *Phys Rev Fluids* 2:094006, DOI 10.1103/PhysRevFluids.2.094006

- Dong B, Yan YY, Li WZ (2011) LBM simulation of viscous fingering phenomenon in immiscible displacement of two fluids in porous media. *Transp Porous Med* 88:293–314, DOI 10.1007/s11242-011-9740-y
- Economides MJ, Nolte KG (2000) *Reservoir Stimulation*, 3rd edn. John Wiley & Sons
- Ferziger JH, Perić M (2002) Solution of the Navier-Stokes Equations. In: *Computational Methods for Fluid Dynamics*, Springer, Berlin/Heidelberg, chap 7, pp 157–216, DOI 10.1007/978-3-642-56026-2{_}7
- Grenfell-Shaw JC, Woods AW (2017) The instability of a moving interface in a narrow tapering channel of finite length. *J Fluid Mech* 831:252–270, DOI 10.1017/jfm.2017.633
- Hill S (1952) Channeling in packed columns. *Chem Eng Sci* 1:247–253, DOI 10.1016/0009-2509(52)87017-4
- Hirt CW, Nichols BD (1981) Volume of fluid (VOF) method for the dynamics of free boundaries. *J Comput Phys* 39:201–225, DOI 10.1016/0021-9991(81)90145-5
- Homsy GM (1987) Viscous fingering in porous media. *Annu Rev Fluid Mech* 19:271–311, DOI 10.1146/annurev.fl.19.010187.001415
- Hu J, Wang B, Sun D (2016) Numerical investigation of viscous fingering in Hele-Shaw cell with spatially periodic variation of depth. *Appl Math Mech-Engl Ed* 37:45–58, DOI 10.1007/s10483-016-2017-9
- Hyman JD, Jiménez-Martínez J, Viswanathan HS, Carey JW, Porter ML, Rougier E, Karra S, Kang Q, Frash L, Chen L, Lei Z, O’Malley D, Makedonska N (2016) Understanding hydraulic fracturing: a multi-scale problem. *Phil Trans R Soc A* 374:20150426, DOI 10.1098/rsta.2015.0426
- Issa RI (1986) Solution of the implicitly discretised fluid flow equations by operator-splitting. *J Comput Phys* 62:40–65, DOI 10.1016/0021-9991(86)90099-9
- Jackson MD, Muggeridge AH, Yoshida S, Johnson HD (2003) Upscaling permeability measurements within complex heterolithic tidal sandstones. *Math Geol* 35:499–520, DOI 10.1023/A:1026236401104
- Jackson SJ, Power H, Giddings D, Stevens D (2017) The stability of immiscible viscous fingering in Hele-Shaw cells with spatially varying permeability. *Comput Meth Appl Mech Engng* 320:606–632, DOI 10.1016/j.cma.2017.03.030
- Jones E, Oliphant T, Peterson P, Others (2001) SciPy: Open source scientific tools for Python. GitHub, URL <http://www.scipy.org/>
- Kim J, Xu F, Lee S (2017) Formation and destabilization of the particle band on the fluid-fluid interface. *Phys Rev Lett* 118:074501, DOI 10.1103/PhysRevLett.118.074501
- Knobloch E, Krechetnikov R (2015) Problems on time-varying domains: Formulation, dynamics, and challenges. *Acta Appl Math* 137:123–157, DOI 10.1007/s10440-014-9993-x
- Lake LW (1989) *Enhanced Oil Recovery*. Prentice Hall, Englewood Cliffs, NJ
- Langer JS (1980) Instabilities and pattern formation in crystal growth. *Rev Mod Phys* 52:1–28, DOI 10.1103/RevModPhys.52.1
- Lindner A, Bonn D, Poiré EC, Ben Amar M, Meunier J (2002) Viscous fingering in non-Newtonian fluids. *J Fluid Mech* 469:237–256, DOI 10.1017/S0022112002001714
- Lu HW, Glasner K, Bertozzi AL, Kim CJ (2007) A diffuse-interface model for electrowetting drops in a Hele-Shaw cell. *J Fluid Mech* 590:411–435, DOI 10.1017/S0022112007008154
- Malhotra S, Sharma MM (2014) Impact of fluid elasticity on miscible viscous fingering. *Chem Eng Sci* 117:125–135, DOI 10.1016/j.ces.2014.06.023
- Maxworthy T (2002) The effect of a stabilising gradient on interface morphology. In: Smith MK, Miksis MJ, McFadden GB, Neitzel GP, Canright DR (eds) *Interfaces for the 21st Century: New Research Directions in Fluid Mechanics and Materials Science*, Imperial College Press, London, pp 3–20

- McCloud KV, Maher JV (1995) Experimental perturbations to Saffman–Taylor flow. *Phys Rep* 260:139–185, DOI 10.1016/0370-1573(95)91133-U
- Miranda JA, Alvarez-Lacalle E (2005) Viscosity contrast effects on fingering formation in rotating Hele-Shaw flows. *Phys Rev E* 72:026306, DOI 10.1103/PhysRevE.72.026306
- Miranda JA, Widom M (1998) Weakly nonlinear investigation of the Saffman-Taylor problem in a rectangular Hele-Shaw cell. *Int J Mod Phys B* 12:931–949, DOI 10.1142/S0217979298000521
- Morrow LC, Moroney TJ, McCue SW (2019) Numerical investigation of controlling interfacial instabilities in non-standard Hele-Shaw configurations. *J Fluid Mech* 877:1063–1097, DOI 10.1017/jfm.2019.623
- Moukalled F, Mangani L, Darwish M (2016) *The Finite Volume Method in Computational Fluid Dynamics: An Advanced Introduction with OpenFOAM® and Matlab*. Fluid Mechanics and its Applications, Springer International Publishing, Cham, Switzerland, DOI 10.1007/978-3-319-16874-6
- Muggeridge A, Cockin A, Webb K, Frampton H, Collins I, Moulds T, Salino P (2014) Recovery rates, enhanced oil recovery and technological limits. *Phil Trans R Soc A* 372:20120320, DOI 10.1098/rsta.2012.0320
- Osiptsov AA (2017) Fluid mechanics of hydraulic fracturing: A review. *J Petrol Sci Eng* 156:513–535, DOI 10.1016/j.petrol.2017.05.019
- Osiptsov AA, Boronin SA, Zilonova EM, Desroches J (2018) Managed Saffman-Taylor instability during overflush in hydraulic fracturing. *J Petrol Sci Eng* 162:513–523, DOI 10.1016/j.petrol.2017.10.018
- Panton RL (2013) *Incompressible flow*, 4th edn. John Wiley & Sons, Hoboken, NJ, DOI 10.1002/9781118713075
- Park CW, Homsy GM (1984) Two-phase displacement in Hele Shaw cells: theory. *J Fluid Mech* 139:291–308, DOI 10.1017/S0022112084000367
- Patankar SV, Spalding DB (1972) A calculation procedure for heat, mass and momentum transfer in three-dimensional parabolic flows. *Int J Heat Mass Transfer* 15:1787–1806, DOI 10.1016/0017-9310(72)90054-3
- Pearson JRA (1960) The instability of uniform viscous flow under rollers and spreaders. *J Fluid Mech* 7:481–500, DOI 10.1017/S0022112060000244
- Pihler-Puzović D, Illien P, Heil M, Juel A (2012) Suppression of complex fingerlike patterns at the interface between air and a viscous fluid by elastic membranes. *Phys Rev Lett* 108:074502, DOI 10.1103/PhysRevLett.108.074502
- Pihler-Puzović D, Périllat R, Russell M, Juel A, Heil M (2013) Modelling the suppression of viscous fingering in elastic-walled Hele-Shaw cells. *J Fluid Mech* 731:162–183, DOI 10.1017/jfm.2013.375
- Pitts E (1980) Penetration of a fluid into Hele-Shaw cell: the Saffman–Taylor experiment. *J Fluid Mech* 97:53–64, DOI 10.1017/S002211208000242X
- Pitts E, Greiller J (1961) The flow of thin liquid films between rollers. *J Fluid Mech* 11:33–50, DOI 10.1017/S0022112061000846
- Popinet S (2018) Numerical models of surface tension. *Annu Rev Fluid Mech* 50:49–75, DOI 10.1146/annurev-fluid-122316-045034
- Rabbani HS, Or D, Liu Y, Lai CY, Lu NB, Datta SS, Stone HA, Shokri N (2018) Suppressing viscous fingering in structured porous media. *Proc Natl Acad Sci USA* 115:4833–4838, DOI 10.1073/pnas.1800729115
- Saffman PG (1986) Viscous fingering in Hele-Shaw cells. *J Fluid Mech* 173:73–94, DOI 10.1017/S0022112086001088

- Saffman PG, Taylor G (1958) The penetration of a fluid into a porous medium or Hele-Shaw cell containing a more viscous liquid. *Proc R Soc Lond A* 245:312–329, DOI 10.1098/rspa.1958.0085
- Tordjeman P (2007) Saffman-Taylor instability of shear thinning fluids. *Phys Fluids* 19:2005–2009, DOI 10.1063/1.2795213
- Vlad DH, Maher JV (2000) Tip-splitting instabilities in the channel Saffman-Taylor flow of constant viscosity elastic fluids. *Phys Rev E* 61:5439–5444, DOI 10.1103/PhysRevE.61.5439
- Wang M, Xiong Y, Liu L, Peng G, Zhang Z (2019) Lattice Boltzmann simulation of immiscible displacement in porous media: Viscous fingering in a shear-thinning fluid. *Transp Porous Med* 126:411–429, DOI 10.1007/s11242-018-1162-7
- Weinstein SJ, Ruschak KJ (2004) Coating flows. *Annu Rev Fluid Mech* 36:29–53, DOI 10.1146/annurev.fluid.36.050802.122049
- Weller HG, Tabor G, Fureby C, Jasak H (1998) A tensorial approach to computational continuum mechanics using object-oriented techniques. *Comput Phys* 12:620–631, DOI 10.1063/1.168744
- Xu F, Kim J, Lee S (2016) Particle-induced viscous fingering. *J Non-Newtonian Fluid Mech* 238:92–99, DOI 10.1016/j.jnnfm.2016.06.014
- Yew CH, Weng X (2014) Proppant transport in a 3D fracture. In: *Mechanics of Hydraulic Fracturing*, 2nd edn, Gulf Professional Publishing, chap 3, pp 49–68, DOI 10.1016/B978-0-12-420003-6.00003-3
- Zhao H, Maher JV (1990) Viscous-fingering experiments with periodic boundary conditions. *Phys Rev A* 42:5894–5897, DOI 10.1103/PhysRevA.42.5894
- Zhao H, Casademunt J, Yeung C, Maher JV (1992) Perturbing Hele-Shaw flow with a small gap gradient. *Phys Rev A* 45:2455–2462, DOI 10.1103/PhysRevA.45.2455
- Zheng Z, Kim H, Stone HA (2015) Controlling viscous fingering using time-dependent strategies. *Phys Rev Lett* 115:174501, DOI 10.1103/PhysRevLett.115.174501
- Zimmerman RW, Bodvarsson GS (1996) Hydraulic conductivity of rock fractures. *Transp Porous Med* 23:1–30, DOI 10.1007/BF00145263

Appendix

To derive the pressure jump at the interface, we first substitute Eq. (8) into Eq. (5) and collect terms at $\mathcal{O}(1)$ to obtain

$$\frac{d^2 p_{0j}}{dx^2} + \frac{3\alpha}{h_{in}} \frac{dp_{0j}}{dx} = 0, \quad j = 1, 2 \quad (\alpha \ll 1). \quad (32)$$

Solving the ordinary differential equation in Eq. (32), we have

$$p_{0j} = C_{1j} e^{-3\alpha x/h_{in}} + C_{2j}. \quad (33)$$

Here, the constants C_{2j} are set by the arbitrary pressure gauge for each fluid; specifically, we can set $C_{2j} = 0$ without loss of generality. (Eq. (3) can also be solved without the linearization in α that leads to Eq. (32) (Pearson, 1960). However, it is not clear whether the significantly more complicated expressions contribute much within the lubrication approximation with $\alpha \ll 1$.) Now, we must specify boundary conditions. At the interface, $x = \zeta = \zeta_0(t) + \mathcal{O}(\epsilon)$, the x -velocities at the leading order (i.e., for an unperturbed interface) must match:

$$\lim_{x \rightarrow \zeta_0^-} u_{x1} = \lim_{x \rightarrow \zeta_0^+} u_{x2} = U(\zeta_0(t)), \quad (34)$$

where U is the local velocity at the interface. Then, using Eqs. (1) and (33), we can re-express Eq. (34) as

$$\lim_{x \rightarrow \zeta_0^-} \frac{dp_{01}}{dx} = - \frac{12\mu_1 U(x)}{[h(x)]^2} \Big|_{x=\zeta_0(t)}, \quad (35a)$$

$$\lim_{x \rightarrow \zeta_0^+} \frac{dp_{02}}{dx} = - \frac{12\mu_2 U(x)}{[h(x)]^2} \Big|_{x=\zeta_0(t)}. \quad (35b)$$

Applying the boundary condition from Eqs. (35) to the solution in Eq. (33), we have

$$p_{0j} = \frac{4\mu_j U(\zeta_0(t)) h_{in}}{\alpha [h(\zeta_0(t))]^2} e^{-\frac{3\alpha}{h_{in}}(x-\zeta_0(t))} \quad (\alpha \ll 1). \quad (36)$$

Similarly, substituting Eqs. (8) and (10) into Eq. (5) and collecting terms at $\mathcal{O}(\epsilon)$, we have

$$\frac{d^2 g_j}{dx^2} + \frac{3\alpha}{h_{in}} \frac{dg_j}{dx} - k^2 g_j = 0, \quad j = 1, 2 \quad (\alpha \ll 1), \quad (37)$$

subject to

$$\lim_{x \rightarrow -\infty} g_1(x) = \lim_{x \rightarrow +\infty} g_2(x) = 0. \quad (38)$$

The solution to Eq. (37) is of the form $g_j = b_{j1} e^{m_1 x} + b_{j2} e^{m_2 x}$, where b_{j1} and b_{j2} are constants, and

$$m_{1,2} = -\frac{3\alpha}{2h_{in}} \left(1 \pm \sqrt{1 + \frac{4k^2 h_{in}^2}{9\alpha^2}} \right). \quad (39)$$

Therefore,

$$g_1(x) = b_{11} e^{m_1 x} + b_{12} e^{m_2 x}. \quad (40)$$

In a diverging cell, $\alpha > 0$, thus $m_1 < 0$ and $m_2 > 0$. From the boundary condition from Eq. (38), $b_{11} = 0$. In a converging cell, $\alpha < 0$, thus $m_1 > 0$, $m_2 < 0$ and $b_{12} = 0$. Hence,

$$g_1(x) = \begin{cases} b_{12} e^{m_2 x}, & \alpha > 0; \\ b_{11} e^{m_1 x}, & \alpha < 0. \end{cases} \quad (41)$$

Similarly,

$$g_2(x) = \begin{cases} b_{21} e^{m_1 x}, & \alpha > 0; \\ b_{22} e^{m_2 x}, & \alpha < 0. \end{cases} \quad (42)$$

Following (Al-Housseiny and Stone, 2013), Eq. (41) and (42) can be combined into a single equation:

$$g_j = \hat{b}(j, \alpha) e^{\hat{m}(j, \alpha)x}, \quad (43)$$

where

$$\hat{m}(j, \alpha) = -\frac{3\alpha}{2h_{in}} \left(1 + (-1)^j \operatorname{sgn}(\alpha) \sqrt{1 + \frac{4k^2 h_{in}^2}{9\alpha^2}} \right), \quad (44)$$

where $\operatorname{sgn}(\alpha) = |\alpha|/\alpha$ for $\alpha \neq 0$ and vanishes otherwise. Therefore, Eq. (10) becomes

$$p_{1j} = \hat{b}(j, \alpha) e^{\hat{m}(j, \alpha)x + iky + \lambda(t)} \quad (\alpha \ll 1). \quad (45)$$

Finally, substituting the leading-order pressure from Eq. (36) and the pressure-correction term from Eq. (45) into the definition of p_j from Eq. (8), leads to

$$p_j(x, y, t) = \frac{4\mu_j U(\zeta_0(t)) h_{in}}{\alpha [h(\zeta_0(t))]^2} e^{-\frac{3\alpha}{h_{in}}(x-\zeta_0(t))} + \epsilon \hat{b}(j, \alpha) e^{\hat{m}(j, \alpha)x + iky + \lambda(t)}. \quad (46)$$

Now, onto the boundary conditions for p_j at the interface. First, consider the kinematic condition, which states that interface velocity equals the fluid velocity at the interface:

$$\frac{\partial \zeta}{\partial t} = \mathbf{u}_j \cdot \hat{\mathbf{n}}|_{x=\zeta(y,t)}, \quad (47)$$

where \mathbf{u}_j is given by Eq. (1). Letting $F = 0$, where $F(x, y) := x - \zeta(y, t)$, implicitly define the interface position, the unit surface normal $\hat{\mathbf{n}}$ can be defined, in Cartesian coordinates, as

$$\hat{\mathbf{n}} = \frac{\nabla F}{\|\nabla F\|} = \frac{1}{\|\nabla F\|} \left(\frac{\partial F}{\partial x}, \frac{\partial F}{\partial y} \right) = \left[1 + \left(\frac{\partial \zeta}{\partial y} \right)^2 \right]^{-1/2} \left(1, -\frac{\partial \zeta}{\partial y} \right). \quad (48)$$

Using a Taylor-series expansion for $|\partial \zeta / \partial y| \ll 1$, we have

$$\begin{aligned} \hat{\mathbf{n}} &= \left(1, -\frac{\partial \zeta}{\partial y} \right) \left[1 - \frac{1}{2} \left(\frac{\partial \zeta}{\partial y} \right)^2 + \mathcal{O} \left(\left(\frac{\partial \zeta}{\partial y} \right)^4 \right) \right] \\ &\simeq \left(1, -\epsilon a e^{iky + \lambda(t)ik} \right), \end{aligned} \quad (49)$$

if only leading-order terms are kept.

Next, we combine Eq. (1) with p_j as given by Eq. (46) to obtain the Darcy velocities

$$\mathbf{u}_j = -\frac{[h(\zeta(t))]^2}{12\mu_j} \left(\frac{\partial p_j}{\partial x}, \frac{\partial p_j}{\partial y} \right), \quad j = 1, 2. \quad (50)$$

Combining Eqs. (49) and (50), we find the normal velocity to be

$$\mathbf{u}_j \cdot \hat{\mathbf{n}} = -\frac{[h(\zeta(t))]^2}{12\mu_j} \left(\frac{\partial p_j}{\partial x} - \frac{\partial p_j}{\partial y} \frac{\partial \zeta}{\partial y} \right). \quad (51)$$

Therefore, each fluid's velocity normal to the interface is given by

$$\mathbf{u}_j \cdot \hat{\mathbf{n}}|_{x=\zeta(y,t)} = U(\zeta_0(t)) + \epsilon \left\{ U(\zeta_0(t)) a \left(\frac{2\alpha}{h(\zeta_0(t))} - \frac{3\alpha}{h_{in}} \right) - \frac{[h(\zeta_0(t))]^2 \hat{b} \hat{m}}{12\mu_j} e^{\hat{m}\zeta_0} \right\} e^{iky + \lambda(t)} + \mathcal{O}(\epsilon^2). \quad (52)$$

Substituting Eq. (7) and Eq. (52) back into Eq. (47), we obtain

$$\hat{b}(j, \alpha) = -\frac{12\mu_j U(\zeta_0(t)) a}{\hat{m}[h(\zeta_0(t))]^2} \left[\frac{\dot{\lambda}}{U(\zeta_0(t))} + \alpha \left(\frac{3}{h_{in}} - \frac{2}{h(\zeta_0(t))} \right) \right] e^{-\hat{m}\zeta_0(t)}. \quad (53)$$

For sufficiently large wave numbers compared to the gap gradient (Al-Housseiny and Stone, 2013), i.e., $|kh_{in}/\alpha| \gg 1$, we can approximate the exponents, given in Eq. (44), as $\hat{m}(1, \alpha) \approx k$ and $\hat{m}(2, \alpha) \approx -k$. Then, the pressure at the interface becomes

$$\begin{aligned} p_j(x, y, t)|_{x=\zeta} &= \frac{4\mu_j U(\zeta_0(t)) h_{in}}{\alpha [h(\zeta_0(t))]^2} \\ &\quad - \epsilon e^{iky + \lambda(t)} \frac{12U(\zeta_0(t)) a}{[h(\zeta_0(t))]^2} \left\{ \mu_j + \left[\frac{\dot{\lambda}}{U(\zeta_0(t))} + \alpha \left(\frac{3}{h_{in}} - \frac{2}{h(\zeta_0(t))} \right) \right] \frac{\mu_j}{\hat{m}(j, \alpha)} \right\} + \mathcal{O}(\epsilon^2). \end{aligned} \quad (54)$$

Thus, finally, the pressure difference across the fluid–fluid interface takes the form of Eq. (11) above.